Dissipation-range geometry and scalar spectra in sheared stratified turbulence

By W I L L I A M D. S M Y T H

College of Oceanic and Atmospheric Sciences, Oregon State University, Corvallis,
OR 97331-5503, USA
e-mail: smyth@oce.orst.edu

Direct numerical simulations of turbulence resulting from Kelvin–Helmholtz instability in stratified shear flow are used to examine the geometry of the dissipation range in a variety of flow regimes. As the buoyancy and shear Reynolds numbers that quantify the degree of isotropy in the dissipation range increase, alignment statistics evolve from those characteristic of parallel shear flow to those found previously in studies of stationary, isotropic, homogeneous turbulence (e.g. Ashurst *et al.* 1987; She *et al.* 1991; Tsinober *et al.* 1992). The analysis yields a limiting value for the mean compression rate of scalar gradients that is expected to be characteristic of all turbulent flows at sufficiently high Reynolds number.

My main focus is the value of the constant q that appears in both the Batchelor (1959) and Kraichnan (1968) theoretical forms for the passive scalar spectrum. Taking account of the effects of time-dependent strain, I propose a revised estimate of q, denoted q_e, which appears to agree with spectral shapes derived from simulations and observations better than do previous theoretical estimates. The revised estimate is $q_e = 7.3 \pm 0.4$, and is expected to be valid whenever the buoyancy Reynolds number exceeds $O(10^2)$. The Kraichnan (1968) spectral form, in which effects of intermittency are accounted for, provides a better fit to the DNS results than does the Batchelor (1959) form.

1. Introduction

Small-scale turbulence in the Earth's atmosphere and oceans is often controlled by a combination of vertical shear and stable density stratification. Shear acts to force turbulence through the medium of Reynolds stresses, while the buoyancy force due to density stratification requires that the flow do work against gravity before vertical motions (and hence Reynolds stresses) can exist. While a large body of theoretical, numerical and laboratory results exists for the simpler case of stationary, homogeneous, isotropic turbulence, the relevance of those results to geophysical turbulence is unclear due to neglect of shear and stratification effects.

My objective here is to extend insights derived from investigations of dissipation-range geometry in stationary, homogeneous, isotropic turbulence (e.g. Ashurst *et al.* 1987; Pope 1990; Tsinober, Kit & Dracos 1992; Reutsch & Maxey 1992; Nomura & Elghobashi 1992; Boratav, Elghobashi & Zhong 1998) to improve understanding of mixing processes in a sheared, stratified environment. The main result is a revised estimate for the adjustable parameter, traditionally denoted q, that appears in theoretical forms of the wavenumber spectrum for a weakly diffusive passive scalar (Batchelor

1959; Kraichnan 1968). This quantity is of central interest, because it represents a timescale for the fundamental process by which turbulence mixes scalar concentrations, namely the sharpening of gradients via compressive strain (see Gibson (1968*a*) for a more complete description of scalar mixing mechanisms). Values obtained from measurements and simulations of geophysical turbulence tend to exceed the existing theoretical estimates by factors of 2–10 (e.g. Dillon & Caldwell 1980; Gargett 1985; Bogucki, Domaradzki & Yeung 1997); my revised estimate attempts to resolve this discrepancy.

The simplest model for sheared, stratified turbulence is that in which the background shear and stratification are constant, both in depth and in time. This allows the maintenance of turbulence that is homogeneous in all three spatial directions and, in certain circumstances, stationary. These idealizations have been approximated in laboratory experiments (Rohr *et al.* 1988; Picirillo & Van Atta 1997) and in several direct and large-eddy simulation studies (Gerz, Schumann & Elghobashi 1989; Holt, Koseff & Ferziger 1992; Kaltenbach, Gerz & Schumann 1994; Jacobitz, Sarkar & Van Atta 1997). In a close antecedent of the present work, Ashurst *et al.* (1987) (also see Nomura & Elghobashi 1992) examined the eigenstructure of the strain tensor in both isotropic flow and flow subjected to a constant shear, but without density stratification.

Constant-gradient models neglect a potentially important source for turbulence, namely the dynamic instability of an inflectional velocity profile (Drazin & Reid 1981). In a stably stratified environment, this mechanism results in the well-known Kelvin–Helmholtz (hereafter KH) instability, which may lead, through a complex sequence of secondary instabilities, to turbulence (see figure 2 of this paper for a graphical summary of the process, or Thorpe (1987) for a detailed review). KH instability has been shown to be important both in the ocean thermocline (Sun, Smyth & Moum 1998) and in stably stratified atmospheric flows (DeSilva *et al.* 1996). Much research on KH instability has been an outgrowth of studies of the related problem of instability of the unstratified mixing layer (e.g. Brown & Roshko 1974; Breidenthal 1981; Rogers & Moser 1992; Moser & Rogers 1991, 1993; Soria *et al.* 1994). Turbulence due to KH instability in stably stratified flow has been the subject of many laboratory experiments (e.g. Thorpe 1973; Koop & Browand 1979; Defina, Lanzoni & Susin 1999). The primary instability and its subsequent evolution in two dimensions were simulated numerically by Patnaik, Sherman & Corcos (1976), Peltier, Halle & Clark (1978), Klaassen & Peltier (1985*a*) and others. Secondary instabilities of finite-amplitude, two-dimensional structures have been explored extensively using linear analysis (e.g. Pierrehumbert & Widnall 1982; Klaassen & Peltier 1985*b*; Smyth & Peltier 1991; Klaassen & Peltier 1991). Recently, computational capacity has increased to the point where fully nonlinear direct numerical simulation (DNS) of the transition to three-dimensional flow is possible (Caulfield & Peltier 1994; Fritts *et al.* 1996; Palmer, Fritts & Andreassen 1996; Cortesi, Yadigaroglu & Banerjee 1998; Cortesi *et al.* 1999; Werne & Fritts 1999).

In this paper, I describe a set of nine direct simulations of turbulent KH billows, beginning with the initial instability and continuing through the transition to turbulence and ultimate return to the parallel state (see Smyth & Moum 1999*a* for further details). This highly non-stationary turbulence is homogeneous in both horizontal directions, but not in the vertical. When turbulence is strongest, the flow is approximately isotropic in the dissipation scales, but not in the energy-containing scales. As turbulence decays, the effects of large-scale anisotropy become evident in the dissipation range (Smyth & Moum 1999*b*). I examine the spatial structure of the

dissipation range via eigenanalyses of the strain tensor, an approach that has been employed profitably in the study of stationary, homogeneous turbulence (Kerr 1985, 1987; Ashurst *et al.* 1987; Vincent & Meneguzzi 1991; She *et al.* 1991; Tsinober *et al.* 1992; Reutsch & Maxey 1992). (An interesting alternative approach is based on the full deformation tensor, e.g. Soria *et al.* 1994.) The focus here is on the evolution of statistical correlations between the scalar gradient field and the principal strains. I examine the evolution of these aspects of dissipation-range structure from a configuration characteristic of stably stratified, parallel flow, to a state of intense turbulence, and back to the parallel state as turbulence decays. Results are tested for dependence on the Reynolds, Richardson and Prandtl numbers.

Particular attention is paid to the evolution of the parameter q, which appears in various theoretical forms for the passive scalar spectrum (e.g. Batchelor 1959; Gibson & Schwarz 1963; Kraichnan 1968). This parameter represents the timescale on which scalar gradients are sharpened by compressive strain, expressed as a multiple of the Kolmogorov eddy turnover time. It turns out that q, as originally defined in terms of the least eigenvalue of the strain tensor by Batchelor (1959), is remarkably constant over a wide range of flow conditions, and that its value is very close to Batchelor's estimate of 2. However, this value is significantly smaller than the range of estimates that have been obtained by fitting observed and computed scalar spectra to the theoretical forms. (These spectrally-derived estimates will be referred to later as q_B and q_K.) The same is true of subsequent theoretical estimates, which include $q < 0.9$ (Kraichnan 1968) and $q = 1.68$ (Newman & Herring 1979). Only the value $q = 4.47$, proposed by Qian (1995), is consistent with observations, and the validity of the theory on which that estimate is based has been questioned (McComb 1990).

A possible explanation for these discrepancies is found via consideration of the effects of non-constant strain. The strain tensor at a material point can vary rapidly in time (e.g. Pope 1990; Yeung, Girimaji & Pope 1990), so that the local scalar gradient never attains the perfect alignment with the direction of maximum compression envisioned by Batchelor. Scalar gradients therefore experience strain that is compressive on average, but less so than the compression represented by the least eigenvalue of the strain tensor. These observations suggest the use of an effective compressive timescale, q_e, defined in terms of the average compression normal to an isoscalar surface. Here, the value of q_e is determined over a wide range of flow regimes, which extends from the strongly-turbulent regime to flows in which turbulence is modified by the effects of buoyancy and large-scale shear. The effective compressive timescale is larger than the ideal value ($q = 2$) suggested by Batchelor (1959), and is in satisfactory agreement with independent estimates made using both computed spectra and geophysical turbulence measurements. I therefore propose that the scalar gradient spectrum in turbulent flow is approximated by the theoretical spectrum of Batchelor (1959) (or, better, the alternative suggested by Kraichnan (1968)) with q replaced by q_e.

I begin in §2 by describing the numerical model used for the simulations and the range of parameter values employed. In §3, I give an overview of the time history of a breaking KH wave: the growth of the instability, the development of turbulence, and the final return to the laminar state. In §4, I explore the statistics of the eigenvalues of the strain tensor, and show how they depend on the degree of anisotropy induced in the dissipation range by large-scale flow geometry. These analyses establish that the dissipation range of the present simulated flows approaches an apparently universal structure provided that the buoyancy Reynolds number is sufficiently large. These results are therefore expected to be characteristic of turbulent flows in general. Section

5 contains the main results of the paper. Statistics of the orientation of the scalar gradient with respect to the principal strains are examined, and the implications for the scalar gradient spectrum are discussed in detail. The present understanding of the spectrum of scalar fluctuations in high Prandtl number flow, which originated with Batchelor (1959), is extended to include the effect of imperfect alignment of the scalar gradient due to non-persistence of the strain field. The resulting estimate of the compression parameter q_e is compared with values derived from my own and other numerical simulations, as well as values estimated from laboratory, atmospheric and oceanographic measurements. The results provide a plausible explanation for the tendency of measured values to significantly exceed Batchelor's estimate. Conclusions are summarized in §6.

2. Methodology

In this section, I describe the mathematical model that we use to represent turbulence in a sheared, stratified environment. I then discuss the numerical methods employed to solve the equations, and the initial conditions for the sequence of simulations whose results are described in the remainder of the paper.

2.1. *The mathematical model*

The mathematical model employs the Boussinesq equations for velocity, density and pressure in a non-rotating physical space measured by the Cartesian coordinates *x*, *y* and *z*:

$$\frac{\partial \boldsymbol{u}}{\partial t} = \boldsymbol{u} \times (\nabla \times \boldsymbol{u}) - \nabla \Pi + g\theta \hat{\boldsymbol{k}} + \nu \nabla^2 \boldsymbol{u}, \tag{1}$$

$$\Pi = \frac{p}{\rho_o} + K. \tag{2}$$

Here, p is the pressure, ρ_o is a constant density scale and $K = \frac{1}{2}\boldsymbol{u} \cdot \boldsymbol{u}$ is the specific kinetic energy. The thermodynamic variable θ represents the fractional specific volume deviation, or minus the fractional density deviation, i.e. $\theta = -(\rho - \rho_o)/\rho_o$, in which ρ_o is a constant mean density. In a fluid where density is controlled only by temperature, θ is proportional to the temperature deviation (with proportionality constant equal to the thermal expansion coefficient). Since this work was motivated by applications to thermally-stratified flow, we will occasionally refer to θ as the temperature. The gravitational acceleration g has the value $9.8 \, \text{m s}^{-2}$, and $\hat{\boldsymbol{k}}$ is the vertical unit vector. Viscous effects are represented by the usual Laplacian operator, with kinematic viscosity $\nu = 1 \times 10^{-6} \, \text{m}^2 \, \text{s}^{-1}$.

The augmented pressure field Π is specified implicitly by the incompressibility condition

$$\nabla \cdot \boldsymbol{u} = 0, \tag{3}$$

and the scalar θ evolves in accordance with

$$\frac{\partial \theta}{\partial t} = -\boldsymbol{u} \cdot \nabla \theta + \kappa \nabla^2 \theta, \tag{4}$$

in which κ represents the molecular diffusivity of θ. Note that the evolution of θ is governed by the same equation that describes the evolution of a passive scalar, even though θ itself is not passive. In other words, any passive scalar that had the same initial distribution as θ, the same diffusivity κ, and was mixed subsequently by the same (buoyancy-modified) flow, would evolve in the same way. This variable

therefore serves a dual purpose, first by imposing realistic buoyancy constraints on the turbulence, and second by mixing in a manner that is characteristic of any scalar quantity one might be interested in.

Periodicity is assumed in the horizontal dimensions:

$$f(x + L_x, y, z) = f(x, y + L_y, z) = f(x, y, z), \tag{5}$$

in which f is any solution field and the periodicity intervals L_x and L_y are constants. At the upper and lower boundaries ($z = \pm\frac{1}{2}L_z$), we impose an impermeability condition on the vertical velocity:

$$w\big|_{z=\pm L_z/2} = 0, \tag{6}$$

and zero-flux conditions on the horizontal velocity components u and v and on θ:

$$\frac{\partial u}{\partial z}\bigg|_{z=\pm L_z/2} = \frac{\partial v}{\partial z}\bigg|_{z=\pm L_z/2} = \frac{\partial \theta}{\partial z}\bigg|_{z=\pm L_z/2} = 0. \tag{7}$$

These imply a vertical boundary condition on Π:

$$\left(\frac{\partial \Pi}{\partial z} - g\theta\right)\bigg|_{z=\pm L_z/2} = 0. \tag{8}$$

2.2. *Initial conditions*

The model is initialized with a parallel flow in which shear and stratification are concentrated in the shear layer, a horizontal layer surrounding the plane $z = 0$:

$$\tilde{u}(z) = \frac{u_o}{2} \tanh \frac{2z}{h_o}, \tag{9}$$

$$\tilde{\theta}(z) = \frac{\theta_o}{2} \tanh \frac{2z}{h_o}. \tag{10}$$

The constants h_o, u_o and θ_o represent the initial thickness of the shear layer and the changes in velocity and density across it. These constants can be combined with the fluid parameters ν and κ and the geophysical parameter g to form three dimensionless groups whose values determine the stability of the flow at $t = 0$:

$$Re_o \equiv \frac{u_o h_o}{\nu}, \quad Ri_o \equiv \frac{g\theta_o h_o}{u_o{}^2}, \quad Pr \equiv \frac{\nu}{\kappa}. \tag{11}$$

The initial macroscale Reynolds number, Re_o, expresses the relative importance of viscous effects. In the present simulations, Re_o is of order a few thousand, large enough that the initial instability is nearly inviscid. The bulk Richardson number, Ri_o, quantifies the relative importance of shear and stratification. If $Ri_o < \frac{1}{4}$, the initial mean flow possesses unstable normal modes (Miles 1961). The Prandtl number, Pr, is the ratio of the diffusivities of momentum and temperature. (This is more properly called the Schmidt number if θ is used to represent some scalar other than temperature.)

In order to obtain a fully-turbulent flow efficiently, I add to the initial mean profiles a perturbation field designed to excite the most-unstable primary and secondary instabilities. The horizontal velocity perturbation is given by

$$\hat{u}(x, z) = \frac{u_o}{2} \frac{1}{k_o} \left(-\cos\frac{2k_o x}{h_o} + 2b\cos\frac{k_o x}{h_o}\right) \tanh\frac{2z}{h_o} \operatorname{sech}\frac{2z}{h_o}, \tag{12}$$

where k_o is the streamwise wavenumber of the fastest-growing eigenmode of the parallel flow. The corresponding vertical velocity perturbation is determined from continuity. This two-dimensional sinusoidal perturbation projects efficiently onto the primary KH instability and the secondary pairing mode (e.g. Klaassen & Peltier 1989). In order to excite three-dimensional secondary instabilities, the spanwise velocity is given a quasi-random perturbation

$$\hat{v}(x, y, z) = \frac{u_o}{2} r_v(x, y, z) \operatorname{sech}^2 \frac{2z}{h_o}, \tag{13}$$

where $r_v(x, y, z)$ is a random function varying between -1 and 1, designed so that $\hat{v}$ will have zero mean and zero vertical integral. Because of the latter condition, it is possible to obtain $\hat{w}(x, y, z)$, the perturbation vertical velocity field corresponding to (12) and (13), simply by integrating (3) in the vertical. Finally, a random perturbation is applied to the scalar field, namely

$$\hat{\theta}(x, y, z) = \frac{\theta_o}{2} r_\theta(x, y, z) \operatorname{sech}^2 \frac{2z}{h_o}, \tag{14}$$

where r_θ is a random function with zero mean, varying between -1 and 1.

The initial condition is now defined by

$$\theta = \tilde{\theta}(z) + a\hat{\theta}(x, y, z), \quad u = \tilde{u}(z) + a\hat{u}(x, y, z),$$
$$v = a\hat{v}(x, y, z), \quad w = a\hat{w}(x, y, z), \tag{15}$$

where a is a constant controlling the amplitude of the initial perturbation.

2.3. *Numerical methods*

Because the horizontal boundary conditions are periodic, discretization of the horizontal differential operators is accomplished efficiently in Fourier space using fast Fourier transforms. In the vertical direction, spatial discretization is done using second-order, centred finite differences, in order to retain flexibility in the choice of upper and lower boundary conditions. The largest-scale runs employ array sizes of $512 \times 64 \times 256$. Although the geometry of the computational grid inevitably excludes some modes that would be present at both large and small scales, it is designed to accommodate those modes which contribute most to the dynamics of the turbulence, allowing us to simulate flows with the highest possible Reynolds number for a given memory capacity.

It is now generally recognized that a reliable DNS code must have grid spacing no greater than a few (3–6) times the Kolmogorov length scale $L_K = (v^3/\epsilon)^{1/4}$ in which ϵ is the volume-averaged kinetic energy dissipation rate (e.g. Moin & Mahesh 1998). For flows with $Pr > 1$, the Kolmogorov scale is replaced by the Batchelor scale: $L_B = L_K/Pr^{1/2}$. In order to take advantage of this information, one must be able to estimate ϵ_+, the effective maximum value of the kinetic energy dissipation rate, in advance. This is done by employing the scaling $\epsilon_+ = cu_o^3/h_o$. This type of scaling for the dissipation rate is standard (e.g. Tennekes & Lumley 1972), but the value of the proportionality constant depends on the definitions chosen for the velocity and length scales. Test simulations have been conducted and have established the value 6.5×10^{-4} for c. The grid spacing is then set to $2.5L_{B-}$ (where L_{B-} is the estimated minimum Batchelor scale $(v^3/\epsilon_+)^{1/4}Pr^{-1/2}$). The smallest resolved scale is approximately $5L_{B-}$ during the most-turbulent phase of flow evolution (when L_{B-} is smallest). In addition to these *a priori* measures, computed fields are monitored

visually for signs of underresolution effects. The present version of the model uses isotropic grid resolution, i.e. $dx = dy = dz$.

The fields are stepped forward in time using a second-order Adams–Bashforth method. Implicit timestepping of the viscous operators has turned out to be unnecessary, as the timestep is limited by the advective terms. For accuracy and numerical stability, the timestep is limited in accordance with

$$\Delta t < 0.12 \min_{i=1,3} \left(\frac{\Delta x_i}{U_i^+} \right), \tag{16}$$

in which U_i^+ is the maximum speed in the x_i coordinate direction. For the present application, the minimum invariably occurs for the streamwise direction $i = 1$. At each timestep, the augmented pressure field is obtained as the solution of a Helmholtz equation which is designed to force the flow to be non-divergent at the next timestep. To reduce aliasing effects, the upper 16% of wavenumbers in each spatial dimension are filtered out of the velocity fields every 1–50 timesteps, depending on the amount of energy present in those modes. This filtering also serves to remove contamination by small-scale pressure modes which arise due to the choice of vertical discretization. The energy removed by filtering is monitored to ensure that it remains small (rarely more than a few percent, never more than 20%) compared with the energy removed by the molecular viscosity term. In the present application, selected scalar quantities are saved at every timestep, while the full three-dimensional fields are saved at intervals of $10h_o/u_o$.

2.4. *Parameter values*

The model equations can be non-dimensionalized using u_o, h_o and θ_o as scales for velocity, length and fractional density fluctuation. The non-dimensional equations are completely specified by the parameter set (Pr, Ri_o, Re_o), and the effects of variations in the values of these three parameters will be of primary concern here. Before discussing them further, however, I will first describe choices for the secondary parameters that appear in the problem.

The boundary conditions, once non-dimensionalized, introduce three additional parameters: L_x/h_o, L_y/h_o and L_z/h_o. Choices for these parameter values must balance the need to maximize Reynolds number with the need to minimize boundary effects. Fortunately, a great deal is known about the large-scale geometry of KH billows, and this allows one to optimize the choice of domain dimensions (e.g. Caulfield & Peltier 1994; Werne & Fritts 1999). These dimensions are based primarily on results from linear stability analyses of the parallel flow (e.g. Hazel 1972; Smyth & Peltier 1989), two-dimensional nonlinear simulations with various domain sizes (Smyth & Peltier 1993) and secondary stability analyses of large-amplitude, two-dimensional KH waves (Klaassen & Peltier 1991). For all runs, I choose $L_x/h_o = 4\pi/k_o h_o = 14.0$, in order to allow for a single pairing of the primary KH wavetrain. This imposes no significant restriction on the flow evolution as long as Ri_o is not too small. Accordingly, I keep $Ri_o \geqslant 0.08$. The vertical domain size L_z/h_o is set to 6.95 for all cases. (More recent simulations with $L_z/h_o = 10.4$ reveal no significant difference in the quantities considered here.) The spanwise domain size is given one of two values: $L_y/h_o = 3.50$ or 1.75, which allow for either four or two (approximate) wavelengths of the dominant secondary instability (Klaassen & Peltier 1991). I believe that two wavelengths is sufficient; four wavelengths were employed in selected runs as a check on this assumption.

The flow evolution is also affected by the initial conditions. Once non-

Run	R12P1	R31P1	R04P7	R08P1	R06P1	R08P4	R21P1	R12P4	R08P7
N_x	256	512	256	256	256	512	512	512	512
N_y	64	64	32	64	64	64	64	64	64
N_z	128	256	128	128	128	256	256	256	256
L_x (m)	3.29	5.24	1.96	3.29	3.29	3.30	5.24	3.29	2.73
L_y (m)	0.82	0.65	0.25	0.82	0.82	0.41	0.66	0.41	0.34
L_z (m)	1.63	2.62	0.98	1.63	1.63	1.64	2.60	1.63	1.36
Δx^3 (10^{-2}m)	1.29^3	1.03^3	0.77^3	1.29^3	1.29^3	0.64^3	1.02^3	0.64^3	0.53^3
h_o (m)	0.236	0.375	0.141	0.236	0.236	0.236	0.375	0.236	0.196
u_o (10^{-3} m s^{-1})	8.34	13.27	4.98	8.34	8.34	8.36	13.27	8.34	8.34
θ_o (10^{-6} K)	2.41	3.83	1.81	3.61	4.81	3.70	5.75	2.41	2.00
Pr	1	1	7	1	1	4	1	4	7
Ri_o	0.08	0.08	0.08	0.12	0.16	0.12	0.12	0.08	0.08
Re_o	1965	4978	701	1967	1967	1977	4978	1967	1354
Re_f	12281	31113	4381	8196	6147	8238	20742	12294	8463

TABLE 1. Parameter values for the simulations. In all cases, $v = 1.0 \times 10^{-6}$ m^2 s^{-1}.

dimensionalized by u_o, h_o and θ_o, these are specified by the wavenumber k_o, the amplitude parameters a and b and by the form of the random noise fields r_v and r_θ. I ignore the slight dependence of k_o on the Richardson number (Hazel 1972) and use $k_o = 0.90/h_o$ for all simulations. The amplitude parameter a appearing in (15) is given the value 0.05, which ensures that the simulation approximates the growth of infinitesimal perturbations, thus minimizing dependence on the precise form of the perturbations. The parameter b, from (12), is given the value 0.4177. This choice dictates that the subharmonic mode will be initialized with one-half the kinetic energy of the primary. Auxiliary runs were conducted to assess the influence of the random noise fields. Although the detailed evolution of the flow is highly sensitive to the initial noise field, the statistical quantities that are of primary concern here are not.

Let us now return our attention to the primary parameters of the problem, namely the Reynolds, Richardson and Prandtl numbers. In the present paper, I describe results from a sequence of nine simulations (table 1) designed to explicate the effects of these three parameters. The first two parameters change as the flow evolves; the third is a property of the fluid and remains constant in time. To explicate the relationships between the time-evolving parameters and their initial values, let us look briefly at the evolution of the Richardson and Reynolds numbers in a typical simulation (figure 1). (These aspects of the flow evolution are described in much greater detail in Smyth & Moum 1999a.)

To define Re and Ri for $t > 0$, one must first define a scale thickness for the evolving mixing layer. This is done in two ways. First, the horizontally-averaged scalar profile, $\bar{\theta}(z)$, is fitted to a piecewise linear function of the form

$$\theta_{pl}(z) = \frac{\theta_o}{2} \begin{cases} 1 & \text{if } z \geqslant \frac{1}{2}h_\theta, \\ z/\frac{1}{2}h_\theta & \text{if } -\frac{1}{2}h_\theta \leqslant z \leqslant \frac{1}{2}h_\theta, \\ -1 & \text{if } z \leqslant -\frac{1}{2}h_\theta, \end{cases} \tag{17}$$

via least squares and thus determines the time-dependent scale thickness for the scalar profile, $h_\theta(t)$. A similar procedure on the horizontally-averaged streamwise
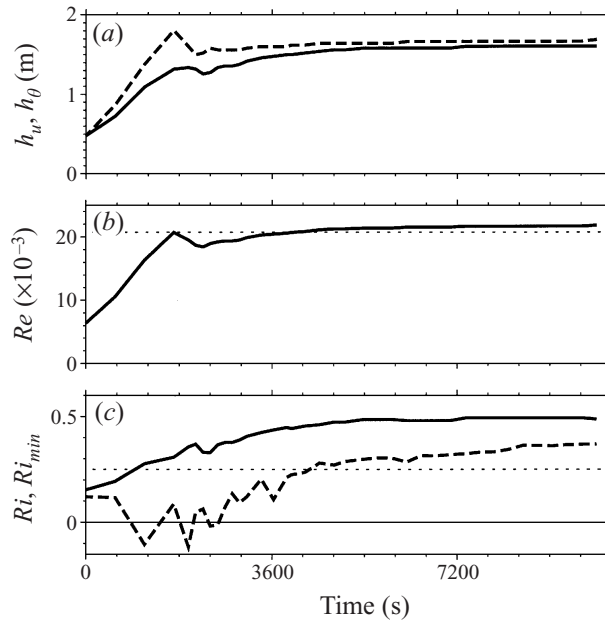
FIGURE 1. Bulk parameters of the mixing layer versus time for a typical simulation, R21P1. (*a*) Velocity scale depth h_u (solid curve) and density depth h_θ (dashed curve). (*b*) Reynolds number based on the layer depth. The horizontal line indicates the estimate $Re_f = 20742$. (*c*) Bulk Richardson number based on the layer depth (solid curve), minimum gradient Richardson number based on horizontally-averaged profiles (dashed curve). Horizontal lines indicate $Ri = 0$ (solid) and $Ri = \frac{1}{4}$ (dashed).

velocity delivers a scale thickness for that profile, namely h_u. These piecewise linear approximations are chosen because they resemble the mean profiles in the fully turbulent regime. Earlier in the evolution, the profiles are closer to the hyperbolic tangent shapes (9) and (10). In particular, h_θ and h_u do not equal h_o at $t = 0$. Although h_θ and h_u asymptote to similar values, h_θ grows more quickly than h_u at early times (figure 1*a*).

An overall thickness scale for the mixing layer is now defined as $h(t) = \frac{1}{2}(h_\theta + h_u)$, and the time-dependent Reynolds and bulk Richardson numbers are based on that scale:

$$Re(t) = \frac{u_o}{\nu}h(t), \quad Ri(t) = \frac{g\theta_o}{u_o^2}h(t). \tag{18}$$

Note that Re and Ri depend on time only through the layer depth, since the net changes in velocity and temperature across the layer are constant. After growing rapidly with the initial instability, the Reynolds number asymptotes towards an approximately-constant value as the flow becomes fully turbulent (figure 1*b*). In this asymptotic regime, turbulent growth of the mixing layer has been effectively arrested by gravity. Continued slow spreading, due mostly to molecular diffusion of the mean profiles, is eventually halted by boundary proximity effects. The analyses are terminated before this point. The bulk Richardson number increases to an asymptotic value close to one half. In contrast, the minimum gradient Richardson number (Ri_{min}) evolves in a complex fashion, often becoming negative during the transition phase as the KH waves overturn.

The asymptotic value of $\frac{1}{2}$ for the bulk Richardson number is a result common to

all of my simulations (to within about 10%), despite a factor of two range in Ri_o. Similarly, the late-time value of Ri_{min} does not vary much from the value $\frac{1}{4}$ for any Ri_o. This means that the main effect of Ri_o, once the transition to turbulence is complete, is to limit the growth of the turbulent layer, and thus the value of Re that is eventually attained. This offers us a valuable simplification: for the flows considered here, we can characterize the turbulent regime using a single parameter, the asymptotic value of the Reynolds number, in place of the two parameters Ri_o and Re_o. A characteristic value for $Re(t)$ in the turbulent regime may be estimated *a priori* using the fact that $Re(t)$ and $Ri(t)$ are both proportional to the layer thickness, $h(t)$, and are therefore proportional to each other. In the asymptotic regime, $Ri \approx \frac{1}{2}$, and the corresponding value for Re is $Re_f = Re_o/2Ri_o$. The estimate Re_f is shown by the dotted line on figure 1(*b*).

In table 1 and throughout this paper, simulations are labelled in terms of the two most important parameters for the turbulent regime, Re_f and Pr. The pattern is 'RxxPy', where 'xx' is $Re_f/1000$ and 'y' is Pr. I will frequently employ run R31P1 to exemplify strong turbulence, R21P1 as an example of a flow that spans a range of turbulent and laminar regimes, and R08P1 as an example of weak turbulence. Conclusions of a more general nature will be based on results from all nine simulations. Results are presented in dimensional form, defined by setting $v = 1.0 \times 10^{-6} \, \text{m}^2 \, \text{s}^{-1}$, a typical value for water.

3. The Kelvin–Helmholtz life cycle

In this section, I give an overview of the evolution of turbulence in selected simulations. The objectives are to provide a conceptual foundation for further analyses, and to establish the degree of isotropy present in the dissipation subrange under different conditions. The turbulence life cycle is illustrated qualitatively in figure 2 by means of isosurfaces of the deformation rate, $d = ((\partial u_i/\partial x_j)(\partial u_i/\partial x_j))^{1/2}$, shown at selected instants in the time evolution of the event. The total physical duration of this simulation is about three hours. In the first frame, it is evident that the initially horizontal layer of vorticity has been concentrated into a pair of KH vortices which are now in the process of merging. At this stage, the flow is almost entirely two-dimensional. The dominant secondary instability has spanwise wavelength equal to one-fourth the spanwise extent of the domain. The signature of this instability is evident in figure 2(*b*). The flow has become significantly three-dimensional, and the fourfold periodicity in the spanwise direction is visible (though it is complicated by the presence of lower harmonics). At the stage shown in figure 2(*c*), the flow is highly disordered, but still exhibits significant symmetry on large scales. In the last stages of billow evolution (figure 2*d*), dissipation is concentrated into quasi-horizontal strips which tend to be thin in the vertical direction and elongated in the streamwise direction. These structures are reminiscent of the 'pancake vortices' often observed in stratified turbulence (e.g. Majda & Grote 1997), but clearly reflect the influence of the background shear. The latter not only contributes directly to the dissipation, but also preferentially amplifies streamwise perturbations (Smyth & Moum 1999*b*).

These processes have been described in detail by Metcalfe *et al.* (1987) and Moser & Rogers (1993) for the unstratified case and by Caulfield & Peltier (1994), Fritts *et al.* (1996), Cortesi *et al.* (1999) and Smyth & Moum (1999*a*) for stratified flow. The example illustrated in figure 2 is one in which the Reynolds number remains relatively small. The higher-Re simulations are similar on the large scales, but develop highly disordered small-scale structures that are most readily examined via statistical analyses.
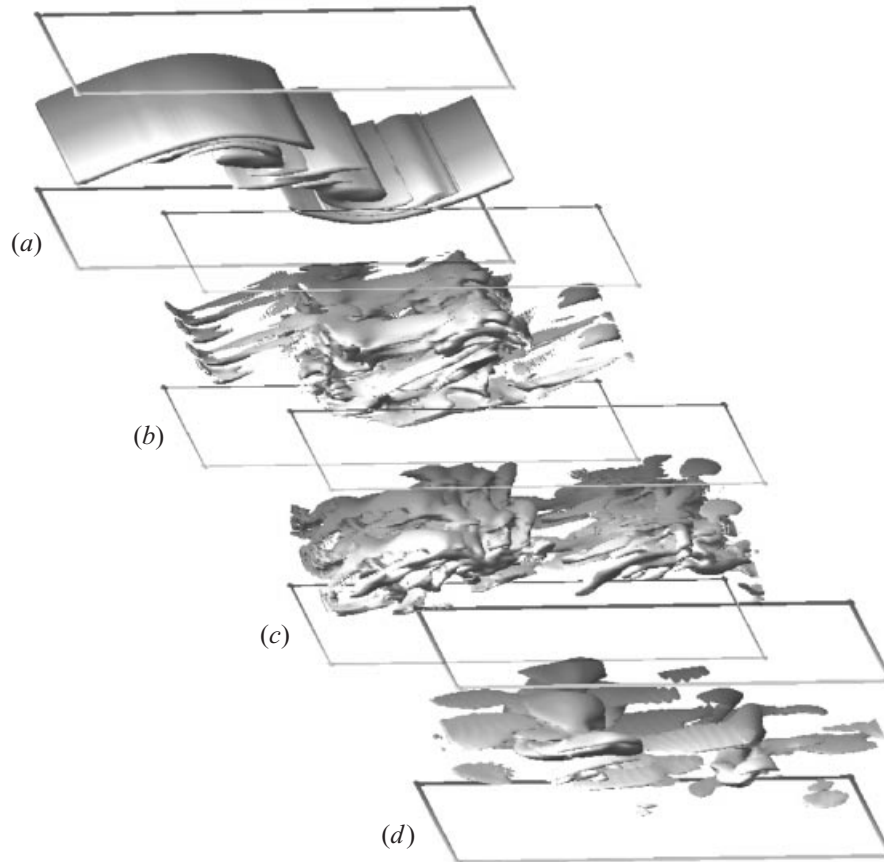
FIGURE 2. Isosurfaces of the deformation rate, d, for run R08P1. (a) $t = 1272$ s, $d = 0.011$ s^{-1}; (b) $t = 2404$ s, $d = 0.036$ s^{-1}; (c) $t = 3252$ s, $d = 0.030$ s^{-1}; (d) $t = 6647$ s, $d = 0.008$ s^{-1}. Gourad shading is used to clarify three-dimensional structure. Graininess in the image represents pixel resolution; grid resolution is much finer. Values of the buoyancy Reynolds number are $Re_b = 7$ (a), 27 (b), 52 (c) and 4 (d).

In figure 3, I illustrate the time-evolution of the three components of the volume-averaged perturbation kinetic energy, $K' = \langle \frac{1}{2}u'^2 \rangle + \langle \frac{1}{2}v'^2 \rangle + \langle \frac{1}{2}w'^2 \rangle$, where primes denote fluctuations about the mean (horizontally-averaged) flow. In order to isolate the most-turbulent regions of the flow and to facilitate the computation of stream-wise wavenumber spectra, volume averages are taken over a thin slab centred on the horizontal midplane of the computational domain, specifically $-L_z/16 < z < L_z/16$. Throughout the paper, this volume average is indicated by angle brackets. I consider the three components of K', $K_x = \langle \frac{1}{2}u'^2 \rangle$, $K_y = \langle \frac{1}{2}v'^2 \rangle$ and $K_z = \langle \frac{1}{2}w'^2 \rangle$, separately. In the early stages of flow evolution, the flow is nearly two-dimensional. The spanwise component of the three-dimensional noise field with which the simulation was initial-ized decays quickly, as is evidenced by the rapid initial decrease of K_y. The horizontal and vertical components grow to a maximum, then enter an oscillatory regime in which the elliptical KH vortex nutates with respect to the mean flow (Klaassen & Peltier 1985a). As the two-dimensional wave reaches maximum amplitude, it becomes unstable to three-dimensional disturbances; beyond this point, the spanwise energy grows rapidly.
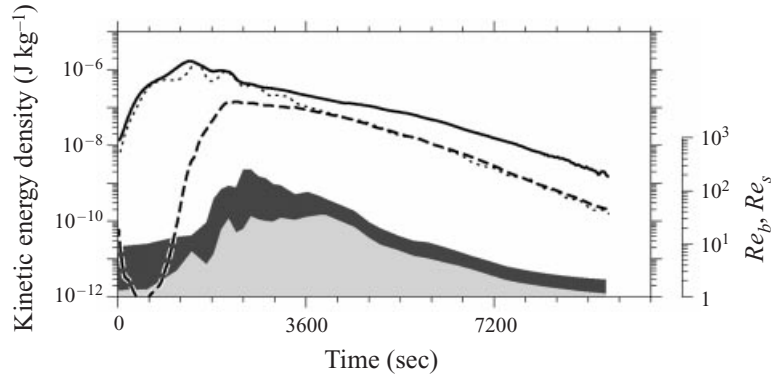
FIGURE 3. Components of the domain-averaged perturbation kinetic energy for run R21P1: K_x (solid), K_y (dashed) and K_z (dotted) versus elapsed time. Also shown are the buoyancy and shear Reynolds numbers $Re_b = \langle\epsilon\rangle/\nu N^2$ (upper shaded curve) and $Re_s = \langle\epsilon\rangle/\nu S^2$ (lower shaded curve). The kinetic energy dissipation rate $\langle\epsilon\rangle$ is computed as a volume average over the layer $-L_z/16 < z < L_z/16$. The velocity and density gradients needed to define N and S are averaged over the same layer.

Also growing during this initial phase are two measures of the instantaneous Reynolds number, both of which will be of central importance in the analyses to follow. The buoyancy Reynolds number is defined by $Re_b = \langle\epsilon\rangle/\nu N^2$, and is a measure of the spectral separation between the Ozmidov length scale $L_O = (\langle\epsilon\rangle/N^3)^{1/2}$ (above which eddies are strongly deformed by stratification) and the Kolmogorov scale $L_K = (\nu^3/\langle\epsilon\rangle)^{1/4}$ (below which eddies are strongly damped by viscosity). The ratio of L_O to L_K is given by $Re_b^{3/4}$. The quantity ϵ that appears in the foregoing expressions is the rate of viscous dissipation of kinetic energy, given at each point in space by

$$\epsilon = 2\nu S_{ij}S_{ij}, \tag{19}$$

in which

$$S_{ij} = \frac{1}{2}\left(\frac{\partial u_i}{\partial x_j} + \frac{\partial u_j}{\partial x_i}\right) \tag{20}$$

is the strain tensor, about which more will be said later. The bulk stratification is represented by $N^2 = g\langle d\theta/dz\rangle$.

One may also estimate the length scale above which eddies are rapidly strained by the background shear: $L_C = (\langle\epsilon\rangle/S^3)^{1/2}$, in which S is the magnitude of the mean vertical shear, $\langle du/dz\rangle$. (The designation L_C is employed in recognition of the early use of this length scale by Corrsin, e.g. Corrsin 1958.) The spectral separation between this and the Kolmogorov scale is represented by the three-fourths power of the shear Reynolds number, $Re_s = \langle\epsilon\rangle/\nu S^2$. In shear-driven turbulence, one expects Re_s to be smaller than Re_b, since the ratio Re_s/Re_b is just the gradient Richardson number, and that quantity must be smaller than $O(1)$ to sustain turbulence. Both Re_b and Re_s tend to be at least an order of magnitude smaller than the macroscale Reynolds number, Re. Also, after attaining maximum amplitude at the transition to turbulence, Re_b and Re_s decay, while Re continues to grow slowly as the mixing layer thickens (figure 1*b*).

The spanwise kinetic energy reaches its maximum near $t = 2400$ s. That maximum is significantly smaller than the current values of K_x and K_y. Subsequently, all three components of the kinetic energy decay monotonically, as do Re_b and Re_s. The vertical kinetic energy K_z, which was similar in magnitude to K_x during the two-dimensional
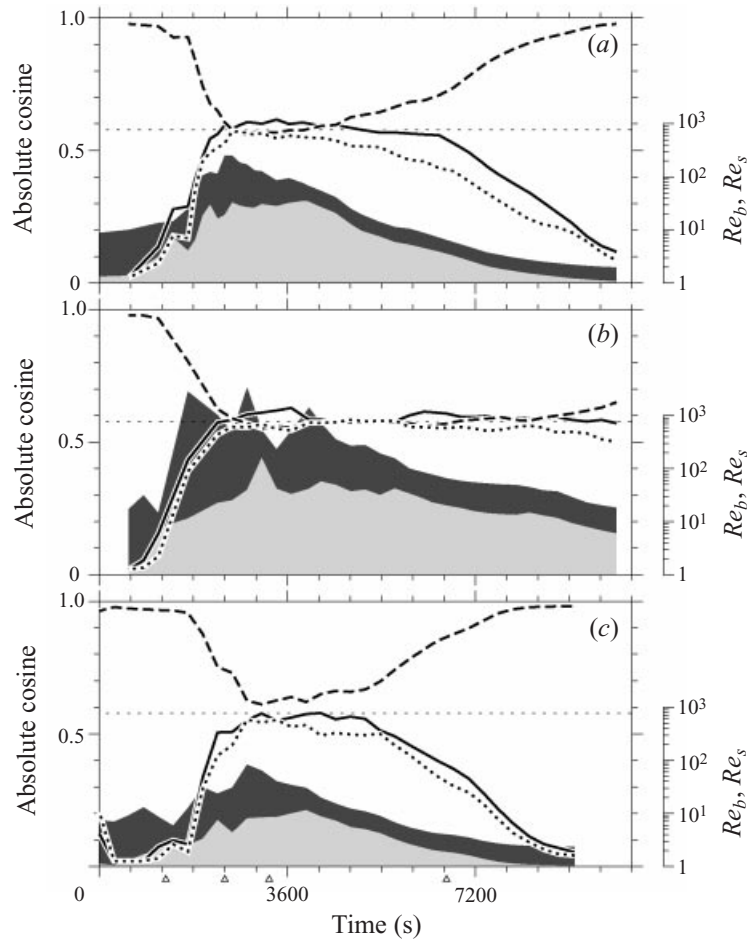
FIGURE 4. Volume-averaged direction cosines of the vorticity vector, $\boldsymbol{\omega} = \nabla \times \boldsymbol{u}$, versus time. The direction cosines are computed as $|\omega_x/\omega|$ (solid curve), $|\omega_y/\omega|$ (dashed curve), and $|\omega_z/\omega|$ (dotted curve), in which ω represents the magnitude of $\boldsymbol{\omega}$. Each quantity is volume-averaged over the layer $-L_z/16 < z < L_z/16$. Horizontal dashed lines indicate the RMS value for an isotropic vector field. Data shown are from simulations R21P1 (*a*), R31P1 (*b*) and R08P1 (*c*). Shaded curves represent Re_b and Re_s as in figure 3. Part (*c*) corresponds to the simulation illustrated in figure 2; symbols below the time axis indicate the times chosen for the latter figure. At two points during R31P1, large-scale overturning leads to $N^2 < 0$ in the central layer. In these flows, L_O is effectively infinite, and the maximum eddy size is determined by the layer depth, h. Accordingly, one defines Re_b as $(h/L_K)^{4/3}$ for these cases.

phase, decays rapidly until it reaches a magnitude similar to that of K_y (at $t = 3600\,\text{s}$). During the long period of viscous decay, K_z and K_y remain nearly equal, while K_x decays slightly more slowly. K_x is an order of magnitude larger than the other two components by the end of the simulation.

Comparison of K_x, K_y and K_z shows clearly that the large scales, in which kinetic energy resides, are highly anisotropic. The mean shear selectively enhances motions in the streamwise direction, while gravity damps vertical motions. At smaller scales, however, one expects to find a regime in which the anisotropy of the large scales is not evident. Such a flow regime is commonly supposed to represent a 'universal'
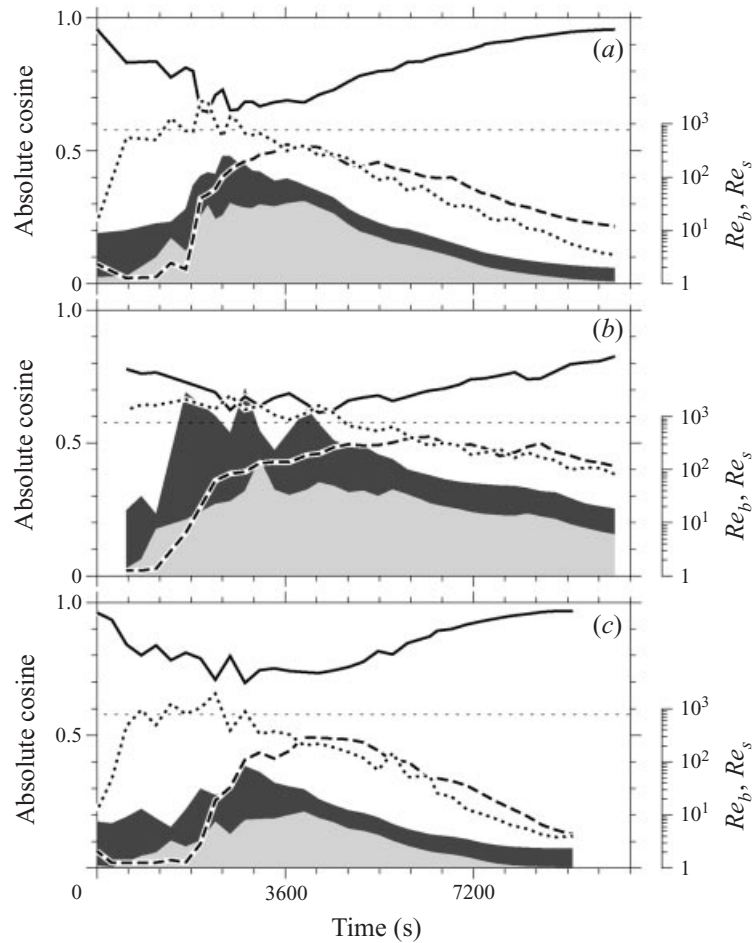
FIGURE 5. Volume-averaged direction cosines of the velocity vector $\boldsymbol{u}$. Data shown are from simulations R21P1 (*a*), R31P1 (*b*) and R08P1 (*c*). Solid curve: $|u|/U$; dashed curve: $|v|/U$; dotted curve: $|w|/U$, in which $U = |\boldsymbol{u}|$. Also shown are the buoyancy and shear Reynolds numbers. All quantities are volume-averaged over the layer $-L_z/16 < z < L_z/16$.

structure which is to some degree independent of the large-scale flow geometry. I next demonstrate that such a regime exists in these simulated flows.

While kinetic energy is carried by large-scale motions, vorticity resides in the smaller scales. This small-scale regime, which also provides the dominant contribution to kinetic energy dissipation, scalar gradients, and scalar variance dissipation, is referred to as the dissipation range. The behaviour of the dissipation range is illustrated in figure 4, which shows the root-mean-square (hereafter RMS) volume averages of the direction cosines of the vorticity vector. If that vector is oriented randomly in space, the three direction cosines are equal and take the value $\sqrt{\frac{1}{3}}$. As the two-dimensional KH instability is growing, the vorticity is aligned almost entirely in the spanwise direction (figure 4*a*, $t < 1800$ s), but the streamwise and vertical components grow rapidly during the transition to turbulence. There follows a phase during which the three cosines are approximately equal, suggesting that the dissipation range is approximately isotropic. As turbulence decays, the vorticity relaxes back to the spanwise orientation characteristic of parallel flow. Figure 4(*b*) shows the same
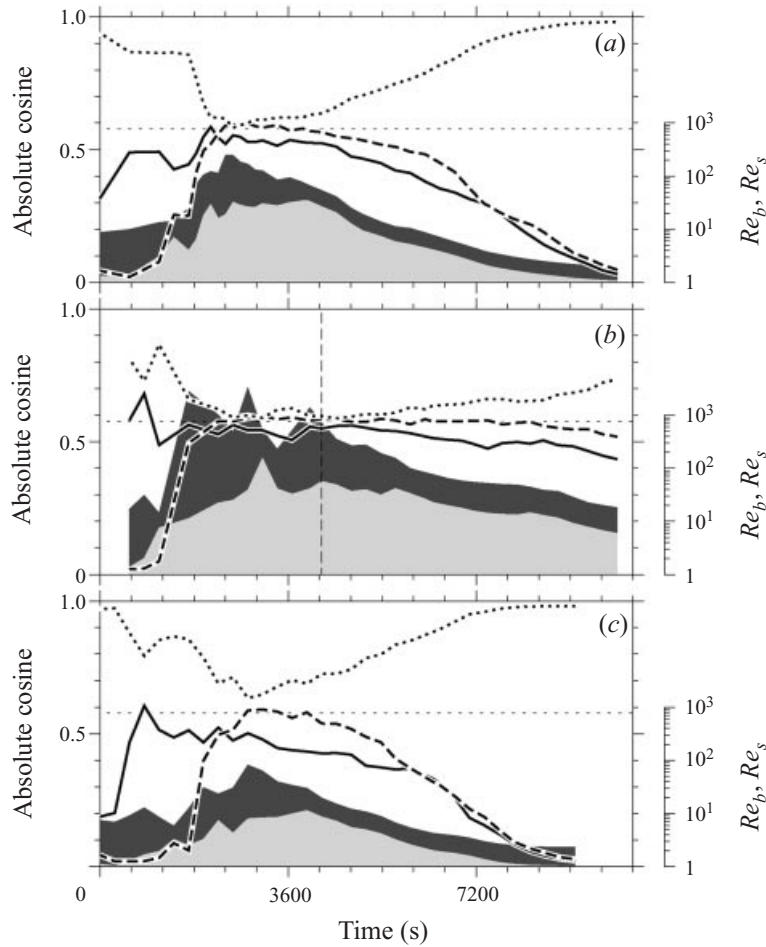
FIGURE 6. Volume-averaged direction cosines of the scalar gradient $\nabla\theta$. Data shown are from simulations R21P1 (*a*), R31P1 (*b*) and R08P1 (*c*). Solid curve: $|\partial\theta/\partial x|/|\nabla\theta|$; dashed curve: $|\partial\theta/\partial y|/|\nabla\theta|$; dotted curve: $|\partial\theta/\partial z|/|\nabla\theta|$. Also shown are the buoyancy and shear Reynolds numbers. All quantities are volume-averaged over the layer $-L_z/16 < z < L_z/16$.

quantities during another simulation, one in which parameters were chosen so as to maximize the Reynolds number. In this case, the isotropic phase lasts much longer; the three direction cosines do not begin to diverge until shortly before the end of the simulation. The third example (figure 4*c*) represents a case of relatively low Re_b, in which isotropy is approached only for a very brief interval after which turbulence decays. (This third example is the simulation illustrated in figure 2.)

For comparison, figure 5 shows the direction cosines of the velocity vector for the same three simulations. In no case does this vector field approach isotropy, illustrating once again the anisotropy of the large scales. The direction cosines of the scalar gradient (figure 6) behave similarly to those of the vorticity, although they relax from the isotropic state slightly faster than do their counterparts in figure 4. As in figure 4, the isotropic state coincides with large values of the buoyancy and shear Reynolds numbers. The vertical dashed line on figure 6 indicates $t = 4242$ s. In the analyses to follow, data from this point in this particular simulation will be used frequently to exemplify the strongly turbulent regime.

It has been shown that, when Re_b and Re_s are sufficiently large, turbulent KH billows develop a dissipation-range in which flow statistics of interest do not reflect the anisotropy present in the large scales. The issue of dissipation-range isotropy is the subject of vigorous debate (e.g. Browne, Antonia & Shah 1987; Thoroddsen & Van Atta 1996), and several authors have pointed out spectrally non-local interactions through which large-scale anisotropy may be reflected in the small scales (e.g. Yeung & Brasseur 1991; Smyth 1992; Mahrt & Howell 1994; Yeung, Brasseur & Wang 1995). The present results do not indicate that such mechanisms are absent, only that these flows approach an asymptotic state, at high Re_b and Re_s, in which the dissipation range is independent of the large scales to a significant degree. The degree of isotropy in the present simulations is discussed in detail in Smyth & Moum (1999*b*), where it is shown via more stringent tests that some degree of anisotropy remains in the dissipation range. The spatial structures of the strain and scalar gradient fields, and their reflection in the form of the scalar gradient spectrum, will be my focus in the remainder of the present paper.

4. Geometry of the strain tensor

The strain tensor (20) has three real eigenvalues, which are traditionally denoted, from largest to smallest, α, β and γ. These quantities are the principal strains. In an incompressible flow,

$$\alpha + \beta + \gamma = 0, \tag{21}$$

so that $\alpha > 0$ (signifying expansion) and $\gamma < 0$ (signifying compression). The intermediate eigenvalue, β, can have either sign. The value of β is a fundamental geometrical property of the turbulence. Positive values of β denote expansion in two dimensions, so that fluid elements tend to be flattened into sheets. When $\beta < 0$, expansion occurs in only one dimension, so that fluid elements tend to be extruded into filaments.

The kinetic energy dissipation rate may be written in terms of the strain tensor:

$$\frac{\epsilon}{\nu} = 2S_{ij}S_{ij} = 2(\alpha^2 + \beta^2 + \gamma^2). \tag{22}$$

This leads to a natural scaling for the eigenvalues in terms of the strain rate of Kolmogorov eddies: $(\alpha, \beta, \gamma) = (\alpha', \beta', \gamma') \times \sqrt{\epsilon/\nu}$. In figure 7(*a*), I show the probability distribution functions for the scaled eigenvalues. This example is from a strongly turbulent flow (simulation R31P1 at $t = 4242$ s, cf. figure 6). The intermediate strain, β', exhibits a marked tendency towards positive values, with mean value 0.08. This distribution function for β' is familiar from previous studies of isotropic turbulence (Kerr 1987; Ashurst *et al.* 1987; She *et al.* 1991). More detailed analyses show that the tendency towards positive β' is stronger in highly dissipative regions of the flow, as has also been found previously (e.g. She *et al.* 1991). The extensional strain eigenvalue, α', is bounded from above by the maximum value $1/\sqrt{3}$, while the compressional strain, γ', tends to lie close to its minimum value, $-1/\sqrt{3}$. The modes of α', β' and γ' are in the proportion (3.1:1:−4.2). For comparison, Ashurst *et al.* (1987) quoted the ratio (3:1:−4), while the wind tunnel experiments of Tsinober *et al.* (1992) yielded (3.1:1:−3.8). Slight differences between these results are most likely due to the vagaries of the mode as a statistical estimator. This close comparison with results from studies of very different flow types indicates that, in the most turbulent regions of space and time, my simulated dissipation range geometry approaches a universal structure.
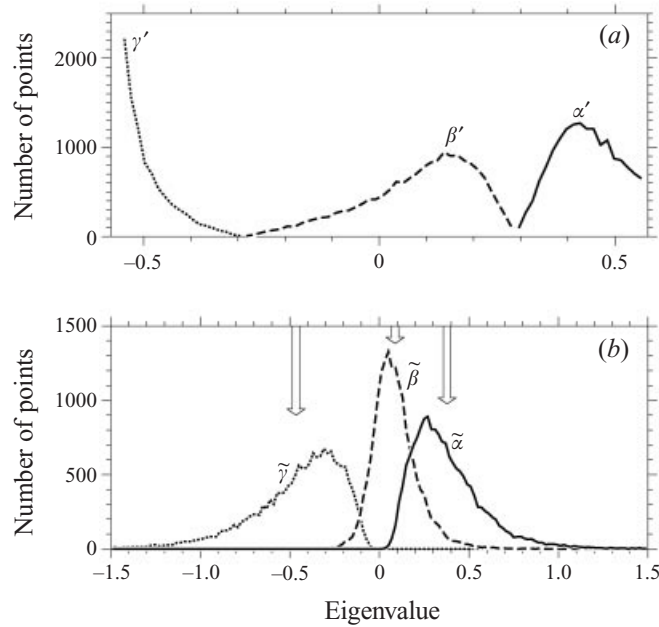
FIGURE 7. Histograms of the eigenvalues of the strain tensor scaled by (a) local and (b) volume-averaged dissipation rates, taken from run R31P1 at $t = 4242$ s, in the layer $-L_z/16 < z < L_z/16$. Solid, dashed and dotted curves represent the extensional, intermediate and compressional eigenvalues, respectively. In (b), arrows indicate the arithmetic mean of each eigenvalue.
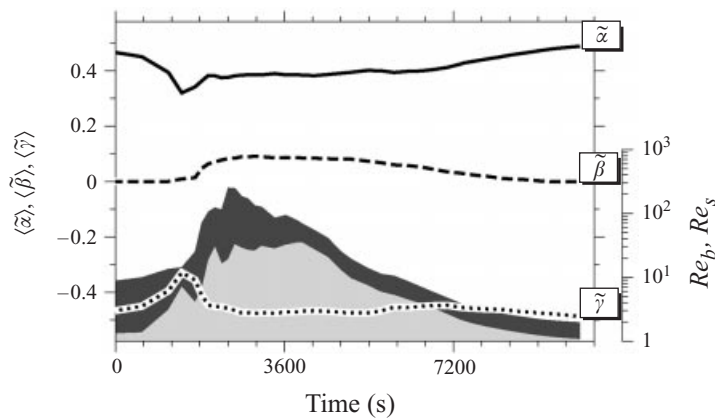

FIGURE 8. Volume-averaged principal strains for run R21P1, normalized using the volume-averaged dissipation rate. Averages are over the layer $-L_z/16 < z < L_z/16$. Shaded curves represent Re_b and Re_s as in figures 3 and 4.

The ultimate goal of this work is to investigate the role of the strain field in shaping the scalar spectrum (cf. §5). For this purpose, one must understand the statistics of the strain field separately from those of the dissipation rate. Therefore, a more relevant scaling for the eigenvalues is that based not on local values of ϵ but rather on a single, volume-averaged value, $\langle\epsilon\rangle$, i.e. $(\alpha, \beta, \gamma) = (\tilde{\alpha}, \tilde{\beta}, \tilde{\gamma}) \times \sqrt{\langle\epsilon\rangle/\nu}$. Probability distribution functions for $\tilde{\alpha}$, $\tilde{\beta}$ and $\tilde{\gamma}$ are shown in figure 7(b). Again, the intermediate strain exhibits a tendency towards positive values. The distribution function for
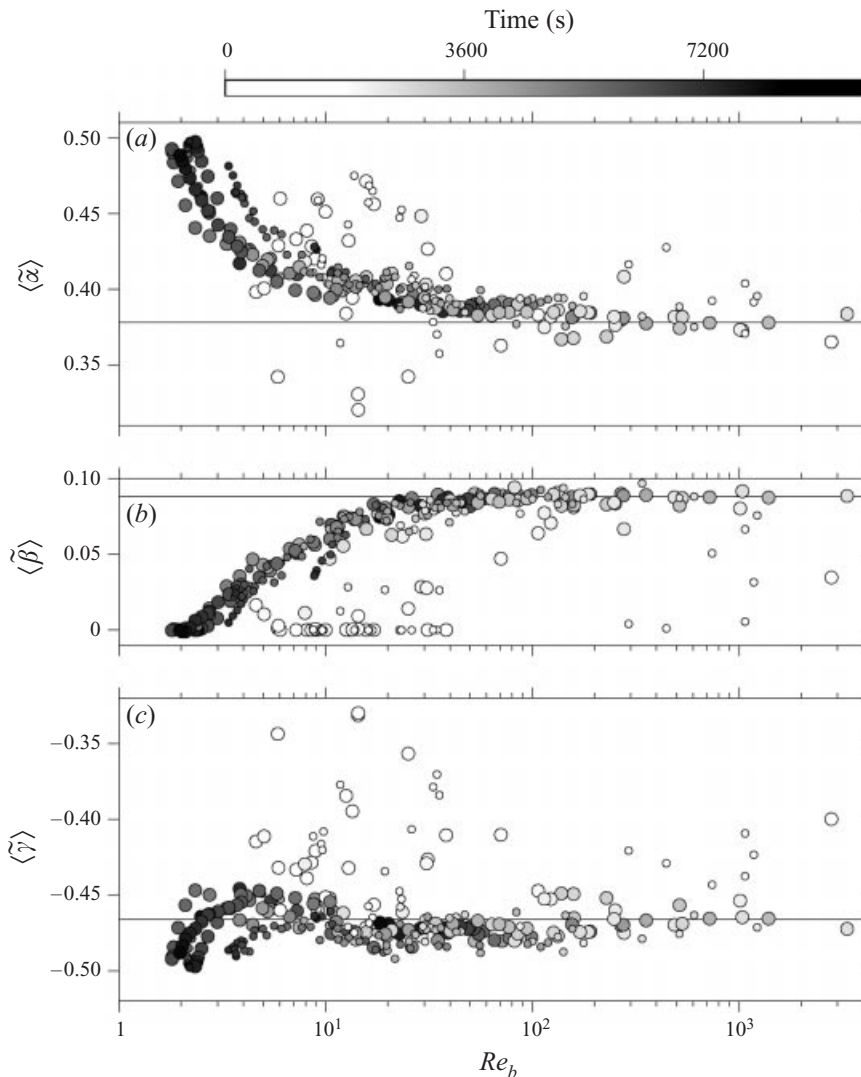
FIGURE 9. Principal strains $\tilde{\alpha}$ (*a*), $\tilde{\beta}$ (*b*) and $\tilde{\gamma}$ (*c*), volume averaged over $-L_z/16 < z < L_z/16$, versus buoyancy Reynolds number, for all simulations. Symbol sizes indicate Prandtl number, with smaller symbols representing $Pr > 1$. The time is indicated by shading, as shown on the bar above (*a*). Horizontal lines indicate the mean values from figure 7(*b*).

the extensional strain eigenvalue, $\tilde{\alpha}$, is highly skewed (in fact, it is approximately lognormal), with most values lying between 0 and 1. The compressional strain, $\tilde{\gamma}$, is more skewed than $\tilde{\alpha}$, with values often lying to the left of -1. The arithmetic means of these scaled strain components are $\langle\tilde{\alpha}\rangle = 0.38$, $\langle\tilde{\beta}\rangle = 0.09$ and $\langle\tilde{\gamma}\rangle = -0.47$.

   This project differs from those quoted above in that I do not attempt to maintain stationary turbulence, but rather allow the flow to evolve to and from the turbulent state in a manner typical of geophysical flows. As a result, I am able to examine the way in which the principal strains reflect these changes in the character of the flow. In simulation R21P1 (figure 8), the volume-averaged principal strains begin with the values $(0.5, 0.0, -0.5)$ characteristic of parallel shear flow. During the initial growth of the KH instability ($0 < t < 1800$ s), $\langle\tilde{\beta}\rangle$ remains close to zero, while $\langle\tilde{\alpha}\rangle$ and

$\langle \tilde{\gamma} \rangle$ decrease sharply in magnitude. This is because the flow remains two-dimensional while $\langle \epsilon \rangle$ increases. As the secondary instability grows and the flow becomes turbulent ($1800 < t < 3000$ s), $\langle \tilde{\alpha} \rangle$ and $\langle \tilde{\beta} \rangle$ and $\langle \tilde{\gamma} \rangle$ approach values similar to those quoted above for the highly isotropic case. The strains then return smoothly to their original values as the flow relaxes back towards the parallel state.

The time dependence of the principal strains is, in fact, closely tied to the time dependences of the buoyancy and shear Reynolds numbers defined in §3 (shaded curves on figure 8). Figure 9 shows scatterplots constructed using data from all nine simulations, illustrating the dependence of the scaled principal strains on Re_b. Before the transition to turbulence (light-shaded circles), the scaled principal strains vary without any apparent pattern while Re_b increases. Transition occurs as Re_b reaches its maximum, after which $\langle \tilde{\alpha} \rangle$, $\langle \tilde{\beta} \rangle$ and $\langle \tilde{\gamma} \rangle$ collapse onto well-defined functions of Re_b as the latter decreases (dark-shaded circles). At large Re_b, there is clear evidence of asymptotic behaviour, i.e. one expects that larger-scale simulations, which would attain higher Re_b after transition than those attained here, would manifest values close to those suggested by the shaded circles on figure 9 ($\langle \tilde{\alpha} \rangle \approx 0.38$; $\langle \tilde{\beta} \rangle \approx 0.09$; $\langle \tilde{\gamma} \rangle \approx -0.47$). There is no evident dependence on the initial values Re_o and Ri_o, or on Pr. Similar analyses using Re_s as the abscissa (not shown) differ only in the fact that Re_s tends to be smaller than Re_b.

I propose the following interpretation of these results. When Re_b is sufficiently large, the effects of large-scale shear and buoyancy are restricted to scales larger than the dissipation subrange (where strain resides), so that the strain-carrying eddies are independent of the large-scale anisotropy. Further increases in Re_b therefore have no effect on the geometry of the dissipation subrange. While principal strains in the low-Re_b regime are characteristic of the parallel flow from which this turbulence evolves, strains in the high-Re_b regime are independent of the large-scale geometry and thus characteristic of all highly-turbulent flows. The results for the high-Re_b regime are entirely consistent with those of the previous investigations cited above, despite the fact that the latter studies spanned a wide variety of flow types. This agreement argues strongly for the universality of the strain eigenvalues in the limit of large Re_b.

5. Compressive strain and the scalar gradient spectrum

I introduce this section with a brief look at scalar spectra from the simulations (§5.1), then examine the statistical relationships between the strain tensor and the scalar gradient that influence the shapes of those spectra (§5.2). I find a revised value for the Batchelor's parameter q that takes account of the time dependence of the strain, and compare the results with simulated and observed scalar spectra (§5.3).

5.1. *Spectra of streamwise scalar gradients in isotropic and anisotropic flow regimes*

The focus in this subsection will be on spectra of streamwise variability, since that direction is homogeneous and is the direction in which the domain (and hence spectral) extent is largest. Let us begin by defining the quantities that will be used to normalize the spectra. An approximation to the scalar variance dissipation rate is

$$\langle \chi_x \rangle = 6\kappa \left\langle \left(\frac{\partial \theta}{\partial x} \right)^2 \right\rangle. \tag{23}$$

This approximation is exact in the isotropic limit (Hinze 1975). For many of the cases to be examined here, the isotropic limit is not approached, and the approximation
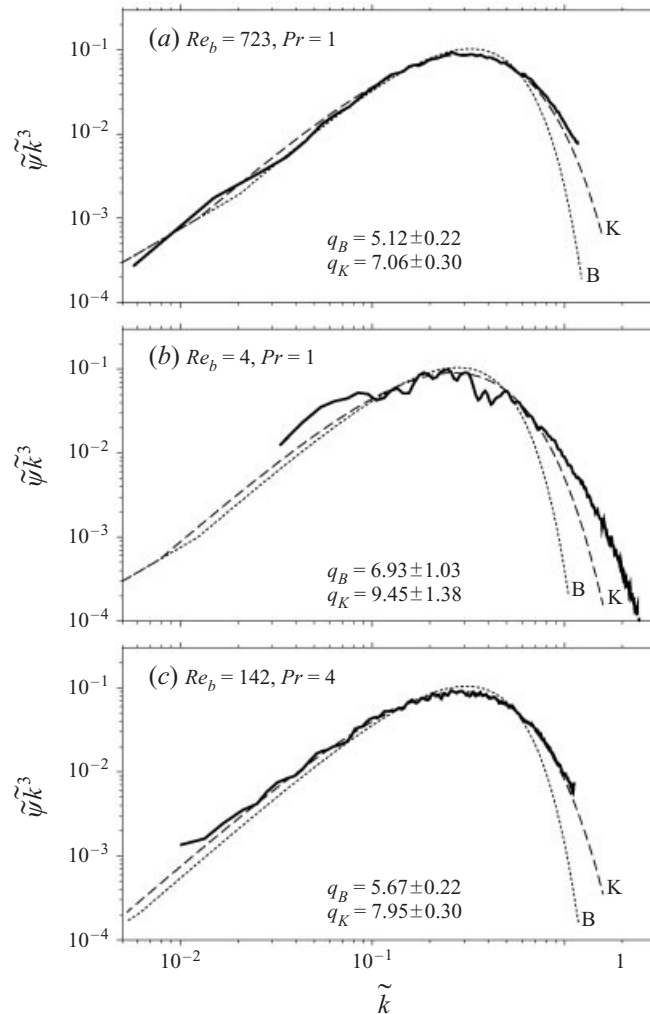
FIGURE 10. One-dimensional scalar spectra as functions of streamwise wavenumber. Both spectra and wavenumber are non-dimensionalized using the Batchelor scaling, then averaged over the middle one-eighth of the vertical extent of the computational domain, $-L_z/16 < z < L_z/16$. The spectra are multiplied by the cube of the scaled wavenumber so as to represent contributions to the scalar gradient in variance-preserving form. Dotted and dashed curves represent the Batchelor and Kraichnan theoretical forms, with values for q_B and q_K obtained by a least-squares fit to the model spectra. (*a*) R31P1, $t = 4242$ s, (*b*) R21P1, $t = 7430$ s, (*c*) R12P4, $t = 3111$ s.

given above underestimates the true dissipation rate, $\langle \chi \rangle$ (Smyth & Moum 1999b). The use of (23) in place of its exact counterpart facilitates interpretation of the results by ensuring that the spectra are at least normalized in a manner consistent with the theoretical forms to which they are compared. I also employ the Batchelor wavenumber, $k_B = (\langle \epsilon \rangle / \kappa^2 v)^{1/4}$. The scalar spectrum, $\psi(k)$, is now defined using the normalization

$$\frac{2\pi}{L_x} \sum_{i=1}^{N_x/2+1} \psi_i = \overline{\theta^2} \qquad (24)$$

where $\psi_i = \psi(k_i)$) and the overbar denotes a horizontal average. The spectrum is non-dimensionalized using the Batchelor scaling

$$\tilde{\psi} = \frac{\psi}{\langle\chi_x\rangle/\kappa k_B^3}, \quad \tilde{k} = \frac{k}{k_B}. \tag{25}$$

Examples are shown in figure 10.

Batchelor (1959) derived a scalar spectrum for a fluid having $Pr \gg 1$ by assuming that scalar gradients were sharpened by a constant, compressive strain. The corresponding one-dimensional scalar gradient spectrum was given by Gibson & Schwarz (1963):

$$\tilde{\psi}_B \tilde{k}^2 = \left(\frac{q_B}{2}\right)^{1/2} \begin{cases} \beta(\frac{1}{2}Prq_B^2)^{-1/3}\zeta^{1/3} & \text{if } \zeta \leqslant \zeta^*, \\ \zeta e^{-\zeta^2/2} - \zeta^2 \int_\zeta^\infty e^{-x^2/2}\,\mathrm{d}x & \text{if } \zeta \geqslant \zeta^*. \end{cases} \tag{26}$$

Here, $\beta \approx 0.6$ is the constant in the Corrsin–Obukhov spectrum for a passive scalar in the inertial-convective subrange (Obukhov 1949; Corrsin 1951). The scaled wavenumber ζ is defined as $(2q_B)^{1/2}\tilde{k}$, and the critical wavenumber ζ^* is determined by the requirement of continuity. The constant q_B was estimated by Batchelor to be equal to the inverse of the spatially-averaged least eigenvalue of the strain tensor, scaled by $(\langle\epsilon\rangle/v)^{1/2}$, or about 2. The latter quantity is referred to here as q. Comparison of the Batchelor spectrum with measured spectra generally indicates that the value 2 is an underestimate of q_B. Gargett (1985) has found values ranging from 4 to 12, and has suggested on that basis that q_B should not be regarded as universal. Gibson (1968b) suggested bounds on q of $[\sqrt{3}, 2\sqrt{3}]\langle\epsilon\rangle^{1/2}/\langle\epsilon^{1/2}\rangle$. The ratio $\langle\epsilon\rangle^{1/2}/\langle\epsilon^{1/2}\rangle$ is at least unity and increases with increasing intermittency (also see Gibson 1982). Gibson (1987) has suggested that the large values of q_B obtained by Gargett (1985) are due to this effect. In the present simulations, it will be shown that q remains close to 2, and that values of q_B in excess of 2 are due to non-persistence of the strain field.

Kraichnan (1968) and Mjolsness (1975) rederived the scalar gradient spectrum allowing for spatial intermittency in the strain rate, and obtained

$$\tilde{\psi}_K \tilde{k}^2 = \left(\frac{q_K}{2}\right)^{1/2} \begin{cases} \beta(\frac{1}{2}Prq_K^2)^{-1/3}\zeta^{1/3} & \text{if } \zeta \leqslant \zeta^*, \\ \zeta e^{-3^{1/2}\zeta} & \text{if } \zeta \geqslant \zeta^*, \end{cases} \tag{27}$$

where q_K is an adjustable constant, $\zeta = (2q_K)^{1/2}\tilde{k}$, and ζ^* is again determined by continuity. Bogucki *et al.* (1997) have shown that scalar spectra from DNS of homogeneous, isotropic, stationary turbulence fit the Kraichnan form (27) better than the Batchelor form (26).

The constants q_B and q_K correspond to the timescale on which compressive strain acts to sharpen scalar gradients, non-dimensionalized by $(\langle\epsilon\rangle/v)^{1/2}$. In the following subsection, I will calculate that timescale explicitly. Here, I obtain q_B and q_K via a nonlinear least-squares fit to the scalar spectrum, in which I minimize the error functional

$$e_B = \sum_{i=1}^{N_x/2+1} \tilde{k}_i^2(\tilde{\psi}_i - \tilde{\psi}_{Bi})^2 \tag{28}$$

(and similarly for q_K). To avoid contamination by the large-scale flow, which is always anisotropic, I do not attempt to fit the portion of the spectrum for which $\tilde{k} < 0.1$. An estimate of the uncertainty in this curve fitting procedure is obtained by repeating the calculation using a slightly different estimate of the central tendency of the spectrum

at each wavenumber. Spectra are again averaged over both horizontal coordinates, but I now combine the results at different z by taking the median rather than the mean. This quantifies the effect that a slightly different, though still reasonable, estimate of the spectrum has on the fitted value of q_B (or q_K).

In the example shown in figure 10(a), q_B and q_K have the values 5.12 ± 0.22 and 7.06 ± 0.30, respectively. The Kraichnan spectrum fits the model results considerably better than does the Batchelor spectrum. This finding is consistent with the results of Bogucki *et al.* (1997), who found superior fits to the Kraichnan spectrum in DNS of stationary, isotropic, homogeneous turbulence. Note in particular that the low-wavenumber range (which was excluded from the least-squares fit) exhibits a clear k^{-1} dependence (i.e. a slope of $+2$). Figure 10(b) shows an example from a flow at considerably lower Re_b. Here, the fit to the theoretical spectra is very poor. This is not surprising, since one expects that the dissipation range will be strongly influenced by buoyancy and large-scale shear in this parameter regime. Note also that the uncertainties in q_B and q_K are large (1.03 and 1.38, respectively), indicating that the fitted values are strong functions of the details of the fitting procedure. The third example is a case of moderate Re_b and high Pr ($Pr = 7$). The fit to the Kraichnan spectrum is once again very good, with value of 7.95 ± 0.30 for q_K.

The results shown in figure 10 are representative of the decay phase for all of the simulations. For small Re_b, the spectrum rolls off more slowly than either of the theoretical forms, and the resulting estimates of q_B and q_K are large and imprecise. The appearance of strong signals at small scales in such cases, e.g. figure 10(b), is an artifact of the approximation (23), which tends to increase $\tilde{\psi}$ to compensate for weak gradients in the streamwise direction when the flow is highly anisotropic. When Re_b is sufficiently large, however, the data fit the Kraichnan spectrum very closely, with values of q_K ranging between 6 and 9.

5.2. *Effects of non-constant strain*

In any flow, the strain field acts to tilt scalar gradients towards an orientation parallel to the compressive eigenvector of the strain tensor. Batchelor's estimate for q_B was based on the assumption that the strain field at a material point evolves slowly compared with the strain rate itself. In such a circumstance, the strain rate may be treated as constant in time, with the effect that scalar gradients remain parallel to the local direction of compressive strain, and thus grow exponentially with growth rate $-\gamma$. Since the non-dimensional strain rate $\langle \tilde{\gamma} \rangle = \langle \gamma \rangle / \sqrt{\langle \epsilon \rangle / \nu}$, is approximately $-\frac{1}{2}$, the non-dimensional compressive timescale, $q = -1/\langle \tilde{\gamma} \rangle$, is approximately 2 (Batchelor 1959).

In reality, the assumption of constant strain is a poor one (e.g. Pope 1990). Strain fields evolve rapidly enough that scalar gradients do not maintain the ideal orientation described above, and therefore do not grow at the optimal rate $-\gamma$. Instead, gradients grow at the rate $-\gamma_e$, where the effective compressive strain γ_e is given at each point in space by

$$\gamma_e = \frac{\nabla\theta \cdot S\nabla\theta}{\nabla\theta \cdot \nabla\theta} = \alpha C_{\theta\alpha}^2 + \beta C_{\theta\beta}^2 + \gamma C_{\theta\gamma}^2. \tag{29}$$

Here, $C_{\theta\alpha}$, $C_{\theta\beta}$ and $C_{\theta\gamma}$ are the cosines of the angles between $\nabla\theta$ and the principal axes $\hat{\boldsymbol{\alpha}}$, $\hat{\boldsymbol{\beta}}$ and $\hat{\boldsymbol{\gamma}}$, respectively. In the limit $(C_{\theta\alpha}, C_{\theta\beta}, C_{\theta\gamma}) \to (0, 0, 1)$, γ_e approaches the ideal value γ. In general, however, $|\gamma_e| < |\gamma|$. In the opposite limit, in which $\nabla\theta$ is oriented randomly with respect to the principal axes, $\langle \gamma_e \rangle = 0$. The effective
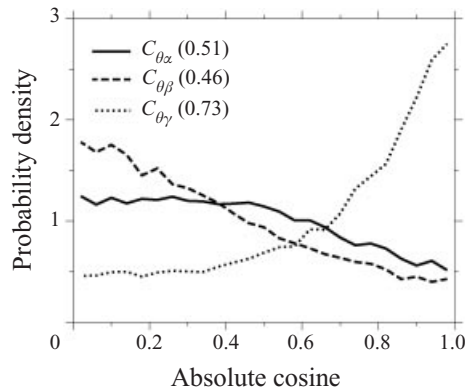
FIGURE 11. Probability density distributions for the direction cosines of the scalar gradient: $C_{\theta\alpha}$ (solid), $C_{\theta\beta}$ (dashed) and $C_{\theta\gamma}$ (dotted). Results pertain to the central layer of the highly turbulent case, run R31P1 at $t = 4242\,\text{s}$. Bracketed numbers indicate the RMS average.

compressive timescale, non-dimensionalized as usual by $(\langle\epsilon\rangle/v)^{1/2}$, is given by

$$q_e = \frac{-1}{\langle\tilde{\gamma}_e\rangle} = \frac{-\sqrt{\langle\epsilon\rangle/v}}{\langle\gamma_e\rangle} \geqslant q. \tag{30}$$

Even in nearly-isotropic flow regimes (e.g. figure 11), the scalar gradient exhibits a preferred range of orientations with respect to the local principal axes. The tendency is for $\nabla\theta$ to be parallel to $\hat{\gamma}$ and perpendicular to $\hat{\alpha}$ and $\hat{\beta}$. This tendency is far from complete, however. The RMS averages of $C_{\theta\alpha}$, $C_{\theta\beta}$ and $C_{\theta\gamma}$ are 0.51, 0.46 and 0.73, respectively. This means that α, β and γ contribute to γ_e in the proportion $(0.5:0.4:1.0)$, an important departure from the proportion $(0:0:1)$ assumed by Batchelor (1959). Using the averaged values shown in figure 11, along with the mean values $\langle\tilde{\alpha}\rangle = 0.38$, $\langle\tilde{\beta}\rangle = 0.09$ and $\langle\tilde{\gamma}\rangle = -0.47$ from §4, in (29), one obtains $-\langle\tilde{\gamma}_e\rangle = 0.13$. The influence of the two extensional strains has thus reduced the compression rate to less than one third of its ideal value, $-\langle\tilde{\gamma}\rangle = 0.47$. This estimate of the effect of non-constant strain on the compression rate of scalar gradients will be developed more fully in the remainder of this section.

To summarize, I have now considered four different estimates of the non-dimensional compressive timescale. The 'ideal' value, q, is defined using the least eigenvalue of the strain tensor, and was employed in the original definition of the Batchelor spectrum. Estimates q_B and q_K are derived by fitting spectra to the Batchelor (1959) and Kraichnan (1968) forms, respectively. The 'effective' value, q_e, is computed from the strain tensor but, unlike q, it takes account of imperfect alignment of the scalar gradient with the compressive strain. My contention will be that q_e provides a better fit to both measured and calculated spectra than does q (i.e. it is closer in value to q_B and q_K).

Let us turn now to an examination of the direction cosines $C_{\theta\alpha}$, $C_{\theta\beta}$ and $C_{\theta\gamma}$ over a range of flow regimes (figure 12). In general, the turbulent regime is characterized by scalar gradients tending towards the direction of the compressional strain, with roughly equal components along the other two principal axes as described above. In the limit of low Re_b, the flow is parallel. The intermediate eigenvalue is zero, and $\hat{\alpha}$ and $\hat{\gamma}$ point at 45° angles from the vertical. The scalar gradient points midway between $\hat{\alpha}$ and $\hat{\gamma}$, which is simply upward. Since $\alpha + \gamma = 0$ in this extreme, the effective strain rate given by (29) vanishes. Note that the departure from isotropic conditions as Re_b
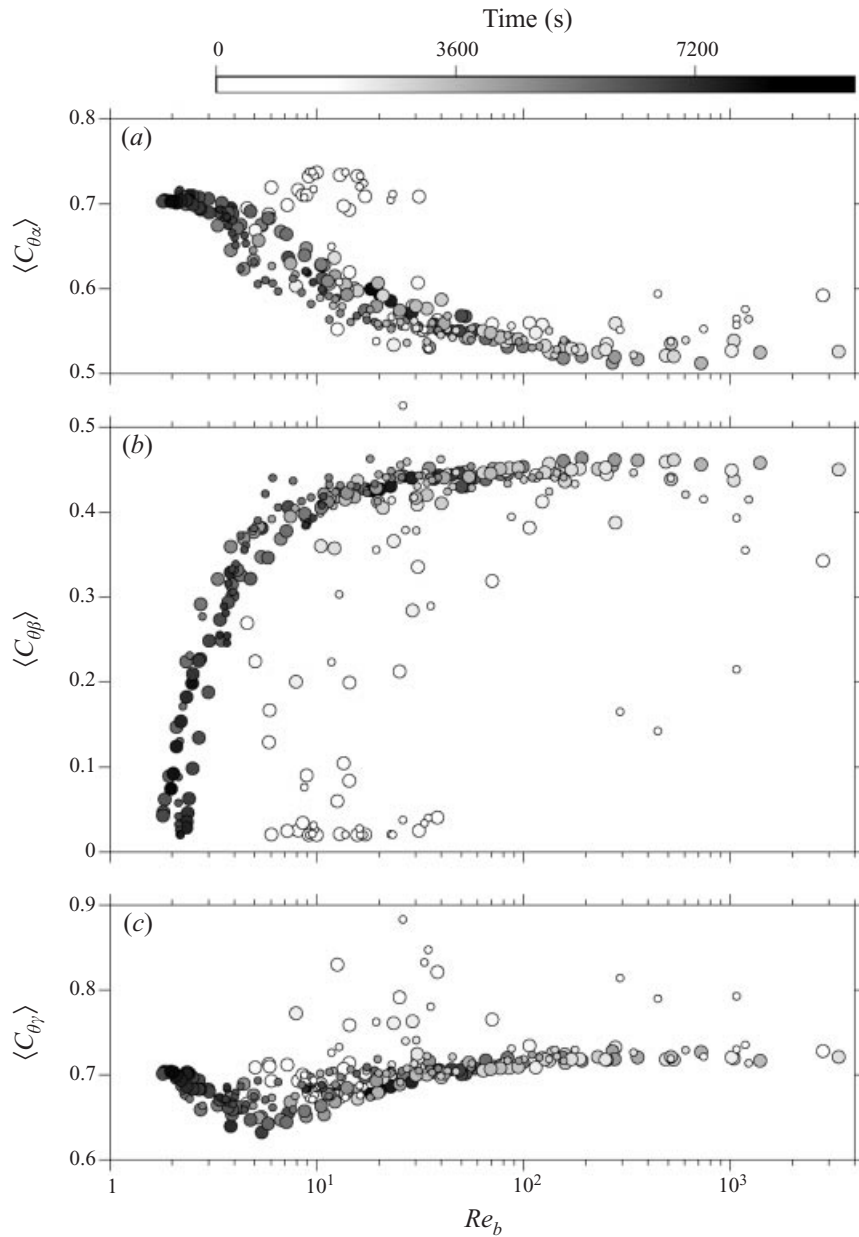
FIGURE 12. Dependences of the absolute cosines (*a*) $C_{\theta\alpha}$, (*b*) $C_{\theta\beta}$ and (*c*) $C_{\theta\gamma}$, upon the buoyancy Reynolds number. Results from all simulations are included. In each case, data are from the central layer $-L_z/16 < z < L_z/16$. Symbol sizes indicate Prandtl number, with smaller symbols representing $Pr > 1$. The time is indicated by shading, as shown on the bar above (*a*).

is reduced tends to occur more gradually in the high-Pr cases than in the $Pr = 1$ cases. This is not surprising: as Re_b decreases, so does L_O, and thus the proportion of the wavenumber spectrum that is larger than L_O increases. Gradients on these large scales are tilted by gravity toward the vertical. On scales smaller than L_O, the tendency is for gradients to tilt towards $\hat{\gamma}$. In the high-Pr cases, there is a relatively
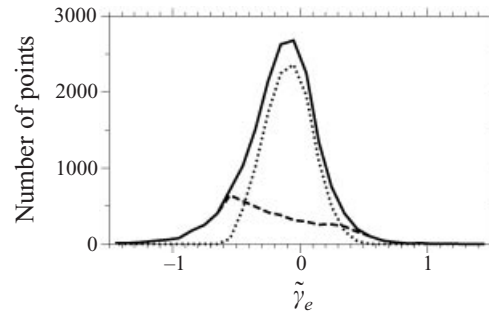
FIGURE 13. Histograms of the non-dimensional, effective compression rate. This example is taken from run R31P1 at $t = 4242$ s; restricted to the central layer $-L_z/16 < z < L_z/16$. Data are subsampled according to the local value of ϵ compared with its volume average, $\langle \epsilon \rangle$. Solid curve: all points; dashed curve: $\epsilon \geqslant \langle \epsilon \rangle$; dotted curve: $\epsilon \leqslant \langle \epsilon \rangle$.

large gradient signal at scales small enough to be dominated by strain rather than buoyancy, and thus a reduced overall tendency for scalar gradients to tilt toward the vertical. From the results illustrated in figure 12, one expects that the effective compression rate $-\langle \tilde{\gamma}_e \rangle$ will drop to zero as Re_b decreases, with the effect appearing first in flows with low Pr.

The spatial statistics of $\tilde{\gamma}_e$ for the isotropic example are shown in figure 13. Note that there is a dramatic difference between the statistics of $\tilde{\gamma}_e$ in highly dissipative regions and those in more quiescent regions. Where the local dissipation rate ϵ exceeds its spatial average, $\tilde{\gamma}_e$ tends to take extreme values, with a preference for strong compression. The mean value of γ_e for this subsample is -0.294. Where ϵ is smaller than its spatial average, $\tilde{\gamma}_e$ takes more moderate values, with only a slight preference for compression (a mean value of -0.096). Since these points are more numerous, however, they dominate the spatial average, so that the overall mean effective compression rate is $\langle \tilde{\gamma} \rangle = -0.158$. The difference between this value and the estimate 0.13 given earlier in this section indicates a positive correlation between large $C_{\theta\gamma}$ and large $\tilde{\gamma}$. This is simply the expected tendency for scalar gradients to align most closely with the compressive direction in highly-compressive regions. The negative reciprocal of the spatially-averaged compression rate provides a representative value for the effective compressional timescale, $q_e = 6.33$.

The foregoing results pertain only to the strongly turbulent case of simulation R31P1 at $t = 4242$ s. I now discuss the dependence of these results on time for the more 'typical' simulation, R21P1 (figure 14). Throughout the life cycle, the ideal compressive timescale, q, remains very close to the value of 2 estimated by Batchelor (1959). In contrast, q_e varies dramatically between the isotropic and anisotropic regimes. In the isotropic regime, q_e approaches the value 6.33 derived above from the high-Re simulation. In anisotropic flow, the effective compression rate is near zero (cf. figure 12 and the accompanying discussion), so that q_e becomes very large.

The time dependence of q_e is closely tied to that of the buoyancy Reynolds number (figure 15). Note first that the ideal compressional timescale, q, does not vary substantially from Batchelor's estimate of 2 at any time, during any simulation, despite wide variations in the Reynolds, Richardson and Prandtl numbers which characterize the flow. Batchelor's estimate therefore proves remarkably robust. The slight increase in q as Re_b is increased is consistent in magnitude with the intermittency effect suggested by Gibson (1968b). In contrast, the effective timescale, q_e, varies greatly
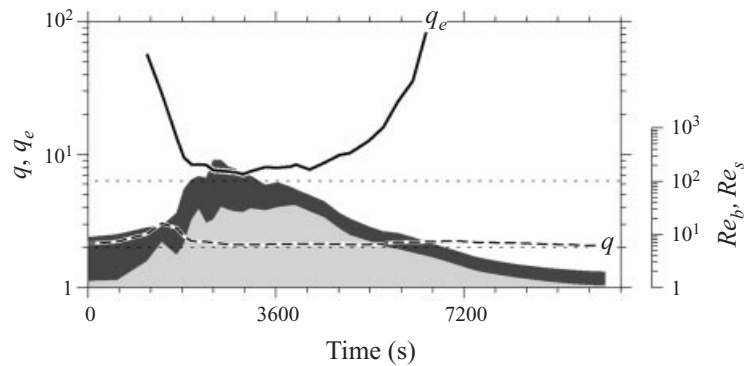
FIGURE 14. Ideal and effective compressive timescales as functions of time. Solid curve: $q_e = -1/\tilde{\gamma}_e$. Dashed curve: $q = -1/\tilde{\gamma}$. Also shown are the buoyancy and shear Reynolds numbers $Re_b = \epsilon/\nu N^2$ (upper shaded curve) and $Re_s = \epsilon/\nu S^2$ (lower shaded curve). This example is run R21P1; data are from the central layer $-L_z/16 < z < L_z/16$.
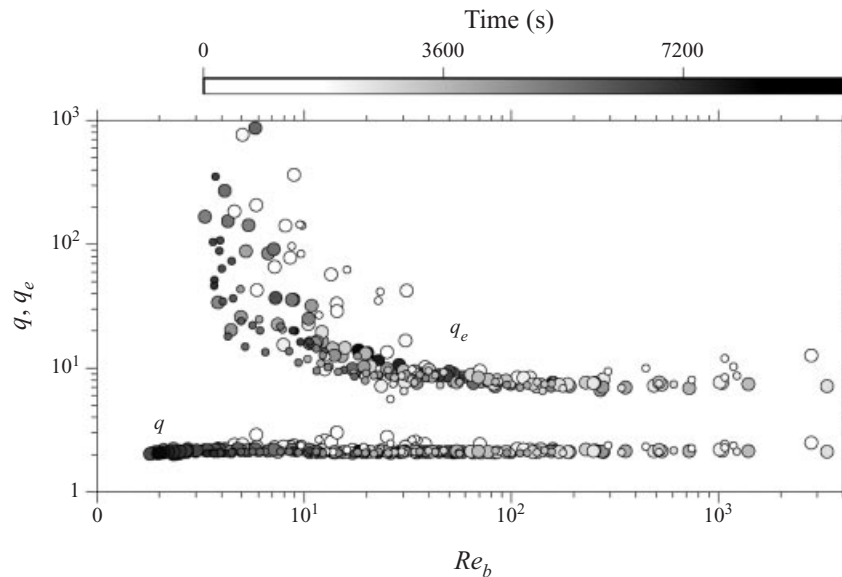

FIGURE 15. Ideal and effective compressive timescales as functions of the buoyancy Reynolds number. Data are taken from all of the simulations listed in table 1. Symbol sizes indicate Prandtl number, with smaller symbols representing $Pr > 1$. The time is indicated by shading. The lower region (where values cluster tightly around 2) is the ideal timescale, q, while the upper region (where data are more variable and scattered) represents the effective timescale q_e.

while never becoming smaller than about 6, even in the large-Re_b limit. Both early and late times are characterized by small Re_b and large q_e. Intermediate times, when turbulence is most intense and Re_b is largest, reveal the smallest values of q_e. The dramatic difference in compressive timescale caused by the fluctuating character of the strain tensor is such that I can plot both the effective and ideal values using the same symbols without fear of confusion. Even in the limit of large Re_b, misalignment between $\nabla\theta$ and $\hat{y}$ due to non-constant strain is sufficient to increase the effective compressive timescale by at least a factor of three above the ideal value 2.

The manner in which q_e diverges from its high-Re_b limit as Re_b decreases is almost

Source	Re_b	q_B	q_K
Predicted value	> 100	—	7.3 ± 0.4
Present spectra	100–1000	4.9 ± 1.0	6.8 ± 1.4
Williams & Paulson (1977)	∞	6	$8^{(b)}$
Bogucki *et al.* (1997)	∞	3.90 ± 0.25	5.26 ± 0.25
Gibson & Schwarz (1963)	∞	2	3
Gargett (1985) A	34000–$63000^{(a)}$	12	$16^{(b)}$
Oakey (1982)	1000–$2000^{(c)}$	3.7 ± 1.5	$4.9 \pm 2.0^{(b)}$
Gargett (1985) B	50–$1750^{(a)}$	4	$5^{(b)}$
Newberger & Caldwell (1981)	$NA^{(d)}$	4.95 (4.28, 6.65)	6.5 (5.6, 8.8)
Grant *et al.* (1968)	$NA^{(d)}$	3.9 ± 1.5	$5.1 \pm 2.0^{(b)}$

TABLE 2. Comparison of numerical and observational estimates of q derived by fitting theoretical spectra. Gargett (1985) A and B refer to the two classes of spectra identified in that paper. Uncertainties represent the standard deviation. [a] Re_b was computed from values of the parameter I given in table 1 of Gargett (1985). [b] Values of q_K from observational data are estimated from the relation $q_K \approx 1.39 q_B$, based on the present results. [c] This range of Re_b was computed from means of the dissipation rates and temperature gradients given in table 2 of Oakey (1982). Salinity effects were neglected. [d] Re_b could not be estimated from the results provided by Newberger & Caldwell (1981) and Grant *et al.* (1968). Newberger & Caldwell (1981) state that the Cox number was > 2000 in the cases they examined, which suggests $Re_b \sim 10^3$ or larger.

certainly specific to the flows simulated here. (Even within this set of simulations, the divergence is visibly slower in the high-Pr cases, as anticipated above.) However, I expect that the asymptotic value of q_e attained at high Reynolds numbers should be common to all turbulent flows. The value 6.33 given earlier is actually one of the lowest values obtained; the more comprehensive results shown in figure 15 suggest that the true limiting value of q_e lies somewhere between 6 and 8. Based on visual examination of figure 15, I estimate that q_e remains within scatter of its asymptotic value for buoyancy Reynolds numbers down to $O(10^2)$, or shear Reynolds numbers down to about 10, and smaller in high-Pr flows. Values of q_e for 23 sample cases in which $Re_b > 100$ and $Re_s > 10$ reveal a mean of 7.3 (with a standard deviation of 0.4). That value is my estimate for the effective non-dimensional compressive timescale of scalar gradients at high Re_b.

A similar calculation has been performed by Yeung *et al.* (1990) for the idealized case of stationary, homogeneous, isotropic turbulence. In that study, the average strain normal to a local material surface was computed following Lagrangian trajectories. Assuming ergodicity, the results ought to be comparable to the present volume-averaged results for large Re_b. The average strain in the highest-Re case considered ($-\langle \gamma_e \rangle$ in the present notation, $\langle a^* \rangle$ in that of Yeung *et al.*) was 0.153 (see their table 2), which corresponds to $q_e = 6.5$. This is somewhat lower than my estimate of 7.3. The discrepancy could easily be due to methodological differences, but it could also indicate that the present results have not quite converged to the high-Re_b limit, and therefore that $q_e = 7.3$ is an overestimate. However, given that I am trying to explain a departure from the 'ideal' value $q = 2$, the discrepancy between 6.5 and 7.3 does not seem important.

5.3. *Comparison with scalar gradient spectra*

Results shown in figure 15 suggest that, when Re_b is decreased below $O(10^2)$, the effective compression rate should increase rapidly towards values exceeding 10^2. This

predicted departure from the isotropic limit does not compare closely with that found by fitting computed spectra to the theoretical forms to obtain q_B and q_K. For the example shown in figure 10(b), the value of q_e is effectively infinite (i.e. the average effective strain is zero). The fitted values of q_B and q_K, while relatively large, are not infinite. This is true in general for the anisotropic flow regime: the fits to the theoretical spectra are very poor, making the estimation of q_B and q_K highly uncertain. The resulting estimates are higher than those found in isotropic cases, but otherwise bear little resemblance to the behaviour of q_e shown on figure 15. It is clear that factors other than the time-dependent strain are influencing the shape of the scalar gradient spectra in this low Reynolds number regime.

In the high-Re_b regime, however, the comparison is excellent. The example shown in figure 10(a) exhibits a close fit to the Kraichnan spectrum, and the resulting value of q_K is 7.0 ± 0.3. This compares very well with the estimate $q_e = 7.3 \pm 0.4$ given in the previous subsection for isotropic flow. For a more detailed comparison, spectra were computed for the 23 cases discussed above (in which $Re_b > 100$ and $Re_s > 10$) and q_B and q_K determined for each. Means were then computed, weighted by the inverse of the uncertainty estimate (cf. §5.1). The resulting mean of q_K is 6.8, with standard deviation 1.4. This agrees with the predicted value to within the statistical uncertainty.

I turn now to comparisons with scalar spectra obtained by other investigators (table 2). Bogucki *et al.* (1997) performed DNS of stationary, homogeneous, isotropic turbulence, and found excellent fits to the Kraichnan spectrum, with $q_K = 5.26 \pm 0.25$. The effective value of Re_b in those unstratified simulations was infinite. Measurements made in geophysical flows have yielded high-quality scalar spectra over a range of Re_b. Fits of the measured spectra to the Batchelor form have yielded values of q_B ranging from 4 to 12 and higher. Explicit comparisons of observational data with the Kraichnan spectrum have not yet been attempted. Spectra measured by Williams & Paulson (1977) in the atmospheric boundary layer and by Oakey (1982) in the upper ocean both appear to roll off less steeply than the best-fit Batchelor curve, suggesting that a closer fit might be achieved using the Kraichnan form. The present results allow one to guess what such a comparison will yield. Estimates of q_K in the 23 samples discussed above exceed the corresponding estimates of q_B by a ratio of 1.39 ± 0.03. I therefore anticipate that fits of observational data to the Kraichnan spectrum (in cases where the fit is reasonably good) will yield values ranging upward from about 5.

Estimates of q_K (and q_B) are widely scattered, and there is no discernible trend with respect to Re_b. In general, the measurements listed in table 2 may be assumed to represent flows with Re_b larger than that achieved in the present simulations. In some cases, estimates of Re_b cannot be made from available information. In both the simulations of Bogucki *et al.* (1997) and the laboratory experiments of Gibson & Schwarz (1963), Re_b was infinite because density stratification was zero. In each case, however, buoyancy effects (i.e. damping of large eddies) may have been mimicked to some degree by the domain boundaries. The large estimates of Re_b that Gargett (1985) assigned to her 'Class A' observations have been questioned by Gibson (1987), who suggests that Gargett's class A measurements are an artifact of extreme inhomogeneity associated with fossil turbulence. Specifically, he suggests that the scalar gradient spectrum is dominated by large regions of the measurement volume in which ϵ (and therefore Re_b) is much smaller than its mean value. If this is true, then the value of ϵ used to scale the spectrum, and the value of Re_b used to interpret the results, may be inappropriately large. Although the characterization of the class A

records as 'fossil' contradicts the observation that the turbulence was newly-created, the inhomogeneity effects suggested by Gibson (1987) nevertheless provide a plausible explanation for the large values of q_B observed. (That problem is not significant in the present results, since the flow is homogeneous by construction in the direction of the spectra.) In summary, it is not clear that a trend in q_K with respect to Re_b could be detected at this point even if it existed. Nevertheless, I conclude that there is nothing in the previous observations to contradict the present suggestion that there is no such trend once $Re_b > O(10^2)$.

As for the asymptotic value of q_K, the present estimate ($q_K = 6.8$) lies slightly towards the high end of the previous estimates listed in table 2, but it is well within the range of those estimates. This remains true even when the Gargett Class A result is excluded. I conclude that the present results are entirely consistent with the net results of existing laboratory, atmospheric, oceanographic and numerical studies. However, I have gone beyond those studies by conducting explicit calculations of the effective strain rate that reinforces scalar gradients. This has enabled me to test Batchelor's view of the physics that govern the scalar spectrum, and to propose a plausible explanation for the tendency of q_B to exceed Batchelor's estimate of 2.

6. Summary

I have documented the contrasting regimes of parallel shear flow and vigorous turbulence with respect to the geometry of the dissipation range. This geometry approaches a clearly-defined asymptotic state, in which the scalar gradient compression rate takes on a characteristic value, as the buoyancy and shear Reynolds numbers become large enough to leave the dissipation range approximately isotropic. In this regime, the large-scale flow geometry is distinctly characteristic of sheared, stratified turbulence forced by KH instability. Yet, the alignment statistics of the dissipation range are consistent with results of previous investigations covering a variety of large-scale flow geometries. These include DNS of stationary, homogeneous, isotropic turbulence (e.g. Yeung *et al.* 1990; She *et al.* 1991), DNS of turbulence subjected to a constant shear (Ashurst *et al.* 1987; Nomura & Elghobashi 1992), and measurements of grid-generated turbulence in a wind tunnel (Tsinober *et al.* 1992). I therefore suggest that this asymptotic behaviour of the dissipation subrange is characteristic of turbulent flows in general.

For the asymptotic regime to be approached to within the scatter of these results, Re_b and Re_s must exceed $O(10^2)$ and $O(10^1)$, respectively. While those values depend to some degree on the large-scale flow geometry, they ought to be valid for a large class of shear-driven buoyancy-damped turbulent flows. Previous studies have indicated that dissipation-range physics is strongly modified by buoyancy effects as Re_b drops below a critical value, estimates of which range between ~ 30 (Gibson 1980) and ~ 100 (Gargett, Osborn & Nasmyth 1984). The present results are consistent with that picture.

In the asymptotic state, the mean compression rate for scalar gradients is $0.16\sqrt{\langle\epsilon\rangle/\nu}$. This result allows me to propose a revised value for the non-dimensional compressional timescale that appears in the Batchelor (1959) and Kraichnan (1968) forms of the scalar spectrum.

Batchelor's theory of scalar fluctuations in the dissipation-range contains four main elements, which I now discuss in turn.

(i) Equilibrium fluctuation strengths are governed by a balance between the effective strain (29) and molecular diffusion. Under appropriate conditions of stationarity,

homogeneity and isotropy, the spectrum should therefore collapse to a universal form when scaled using the length scale $L_B = (\kappa/\langle|\gamma_e|\rangle)^{1/2}$. The present results favour universality, although this property of the scalar spectrum remains controversial (e.g. Gargett 1985).

(ii) Assuming that the effective strain rate is statistically sharp, Batchelor (1959) derived a specific functional form for the proposed universal spectrum. Kraichnan (1968) relaxed Batchelor's assumption using the Lagrangian History Direct Interaction Approximation, and thereby derived a revised functional form that accounts for intermittency effects. While Batchelor's form rolls off like a Gaussian at high wavenumbers, Kraichnan's form exhibits a gentler, exponential roll-off. Both forms exhibit k^{-1} subranges at lower wavenumbers. The present spectra (at sufficiently large Re_b) exhibit the k^{-1} range, along with a gentle roll-off at high wavenumbers that indicates a preference for the Kraichnan form.

(iii) Because the effective strain rate is difficult to measure, Batchelor suggested a parameterization in terms of the mean dissipation-rate: $\langle\gamma_e\rangle = -q_e^{-1}(\langle\epsilon\rangle/v)^{1/2}$. This leads to the more familiar expression $L_B = (\kappa^2 v/\langle\epsilon\rangle)^{1/4}$ for the Batchelor length scale. Gibson (1968b) pointed out that a more physically appropriate parameterization would employ $\langle\epsilon^{1/2}\rangle$ rather than $\langle\epsilon\rangle^{1/2}$. Because only the latter can be measured in most cases, subsequent investigators have retained Batchelor's form. In the present results, the difference between $\langle\epsilon^{1/2}\rangle$ and $\langle\epsilon\rangle^{1/2}$ is at all times less than 15%.

(iv) To estimate a value for q_e, Batchelor equated γ_e with the least principal strain, γ, in which case $q_e = q$. In other words, the scalar gradient field was assumed to be aligned perfectly with the compressive eigenvector of the strain tensor, as would occur in the long-time limit if the strain field was steady. Using contemporary measurements of γ, Batchelor then arrived at the estimate $q_e \approx q \approx 2$. My results confirm that $q \approx 2$, but also indicate that q_e is substantially greater than q, as do most of the spectral estimates listed in table 2.

In the present study, the emphasis is on the fourth item listed above. My goal has been to relax the assumption of perfect alignment between the scalar gradient field and the compressive strain, taking advantage of the possibility of computing alignment statistics using DNS data. The particular alignment statistic needed, $\langle\gamma_e\rangle$, was first computed for the case of purely homogeneous, isotropic turbulence by Yeung *et al.* (1990). I have shown, through the consistency of q_e and q_K, that this effective strain rate is very close to the value needed to explain the shape of the scalar spectrum in the dissipation range. I have also estimated the minimum values that the buoyancy and shear Reynolds numbers must take in order for the requirements of dissipation-range homogeneity and isotropy to be satisfied in a sheared, stratified environment typical of geophysical flows.

The conclusions are as follows. For $Re_b > O(10^2)$, or $Re_s > O(10^1)$, the scalar spectrum has the Kraichnan (1968) form (27), with $q_K = 6.8 \pm 1.4$. This value of q_K is predicted accurately by Batchelor's parameterization of the effective strain, once the imperfect alignment between the scalar gradient and the compressive strain is accounted for. Direct computation of the effective compression rate gives $q_e = 7.3 \pm 0.4$.

Previous estimates of q_B have yielded widely scattered results ranging from 2 (Gibson & Schwarz 1963) to 12 (Gargett 1985), which correspond to q_K ranging from 3 to 16. The reason for the scatter is not understood. It could be that the scalar spectrum is not universal after all, as suggested by Gargett (1985). As further support for this possibility, I note that both the atmospheric observations of Mahrt & Howell (1994) and the simulations of Yeung *et al.* (1995) and Smyth & Moum (1999b) suggest that higher-order statistics may reveal anisotropy imposed on the dissipation

range by large-scale geometry, even though such anisotropy is not evident in analyses like those considered here. It could also be that the ideal conditions of stationarity, homogeneity and isotropy upon which universality depends are not present in some of these flows. The absence of stationarity is difficult to recognize in observational data, and could result in spectra far from the equilibrium form. Inaccurate estimates of $\langle \epsilon \rangle$ may result from inhomogeneity (e.g. Gibson 1987) or from anisotropy (Itsweire *et al.* 1993; Smyth & Moum 1999*b*). Finally, the discrepancies could simply reflect the inherent difficulty of fitting the theoretical curves to observational data (cf. § 5.1, also Oakey 1982). Ongoing research is addressing the various mechanisms that may influence estimates of q_B and q_K.

The present results are consistent with the existing observational, experimental and numerical data. My estimate of q_B lies well within the range of previous estimates (cf. table 2). Like most previous measurements, my estimate significantly exceeds that of Batchelor (1959), and an explanation for that has been proposed. My conclusion that the high Reynolds number limit is reached when Re_b exceeds $O(10^2)$ would be invalidated if previous measurements of q_B showed a trend with respect to Re_b, but they do not. The available evidence therefore suggests that mismatches between measured scalar spectra and the theoretical form of Batchelor (1959) are due to non-persistence of the strain field and the resulting misalignment of the scalar gradient with the compressive strain.

REFERENCES

Ashurst, W., Kerstein, A., Kerr, R. & Gibson, C. 1987 Alignment of vorticity and scalar gradient with strain rate in simulated Navier–Stokes turbulence. *Phys. Fluids* **30**, 2343–2353.

Batchelor, G. K. 1959 Small-scale variation of convected quantities like temperature in turbulent fluid. *J. Fluid Mech.* **5**, 113–133.

Bogucki, D., Domaradzki, J. & Yeung, P. 1997 Direct numerical simulations of passive scalars with $Pr > 1$ advected by turbulent flow. *J. Fluid Mech.* **343**, 111–130.

Boratav, O., Elghobashi, S. & Zhong, R. 1998 On the alignment of strain, vorticity and scalar gradient in turbulent, buoyant, nonpremixed flames. *Phys. Fluids* A **10**, 2260–2267.

Breidenthal, R. 1981 Structure in turbulent mixing layers and wakes using a chemical reaction. *J. Fluid Mech.* **109**, 1–24.

Brown, G. & Roshko, A. 1974 On density effects and large structure in turbulent mixing layers. *J. Fluid Mech.* **64**, 775–816.

Browne, L., Antonia, R. & Shah, D. 1987 Turbulent energy dissipation in a wake. *J. Fluid Mech.* **179**, 307–326.

Caulfield, C. & Peltier, W. 1994 Three-dimensionalization of the stratified mixing layer. *Phys. Fluids* A **6**, 3803–3805.

Corrsin, S. 1951 On the spectrum of isotropic temperature fluctuations in isotropic turbulence. *J. Appl. Phys.* **22**, 469–473.

Corrsin, S. 1958 Local isotropy in turbulent shear flow. *NACA RM* 58B11.

Cortesi, A., Smith, B., Yadigaroglu, G. & Banerjee, S. 1999 Numerical investigation of the

entrainment and mixing processes in neutral and stably-stratified mixing layers. *Phys. Fluids* A **11**, 162–185.

CORTESI, A., YADIGAROGLU, G. & BANERJEE, S. 1998 Numerical investigation of the formation of three-dimensional structures in stably-stratified mixing layers. *Phys. Fluids* A **10**, 1449–1473.

DEFINA, A., LANZONI, S. & SUSIN, F. 1999 Stability of a stratified viscous shear flow in a tilted tube. *Phys. Fluids* A **11**, 344–355.

DESILVA, I., FERNANDO, H., EATON, F. & HEBERT, D. 1996 Evolution of Kelvin–Helmholtz billows in nature and laboratory. *Earth Planet. Sci. Lett.* **143**, 217–231.

DILLON, T. & CALDWELL, D. 1980 The Batchelor spectrum and dissipation in the upper ocean. *J. Geophys. Res.* **85** (C4), 1910–1916.

DRAZIN, P. & REID, W. 1981 *Hydrodynamic Stability*. Cambridge University Press.

FRITTS, D., PALMER, T., ANDREASSEN, O. & LIE, I. 1996 Evolution and breakdown of Kelvin–Helmholtz billows in stratified compressible flows. Part 1: Comparison of two- and three-dimensional flows. *J. Atmos. Sci.* **53**, 3173–3191.

GARGETT, A. 1985 Evolution of scalar spectra with the decay of turbulence in a stratified fluid. *J. Fluid Mech.* **159**, 379–407.

GARGETT, A., OSBORN, T. & NASMYTH, P. 1984 Local isotropy and the decay of turbulence in a stratified fluid. *J. Fluid Mech.* **144**, 231–280.

GERZ, T., SCHUMANN, U. & ELGHOBASHI, S. 1989 Direct numerical simulation of stratified homogeneous turbulent shear flows. *J. Fluid Mech.* **200**, 27–45.

GIBSON, C. 1968a Fine structure of scalar fields mixed by turbulence. I. Zero gradient points and minimal gradient surfaces. *Phys. Fluids* **11**, 2316–2327.

GIBSON, C. 1968b Fine structure of scalar fields mixed by turbulence. II. Spectral theory. *Phys. Fluids* **11**, 2316–2327.

GIBSON, C. 1980 Fossil temperature, salinity and vorticity turbulence in the ocean. In *Marine Turbulence* (ed. J. Nihoul), pp. 221–257. Elsevier.

GIBSON, C. 1982 Fossil turbulence in the Denmark Strait. *J. Geophys. Res.* **87** (C10), 8039–8046.

GIBSON, C. 1987 Fossil turbulence and intermittency in sampling oceanic mixing processes. *J. Geophys. Res.* **92**, 5383–5404.

GIBSON, C. & SCHWARZ, W. 1963 The universal equilibrium spectra of turbulent velocity and scalar fields. *J. Fluid Mech.* **16**, 365–384.

GRANT, H. L., HUGHES, B., VOGEL, W. & MOILLIET, A. 1968 The spectrum of temperature fluctuations in turbulent flow. *J. Fluid Mech.* **34**, 423–442.

HAZEL, P. 1972 Numerical studies of the stability of inviscid parallel shear flows. *J. Fluid Mech.* **51**, 39–62.

HINZE, J. 1975 *Turbulence*, 2nd edn. McGraw-Hill.

HOLT, S., KOSEFF, J. R. & FERZIGER, J. 1992 A numerical study of the evolution and structure of homogeneous stably stratified sheared turbulence. *J. Fluid Mech.* **237**, 499–539.

ITSWEIRE, E., KOSEFF, J., BRIGGS, D. & FERZIGER, J. 1993 Turbulence in stratified shear flows: Implications for interpreting shear-induced mixing in the ocean. *J. Phys. Oceanogr.* **23**, 1508–1522.

JACOBITZ, F., SARKAR, S. & VAN ATTA, C. 1997 Direct numerical simulations of the turbulence evolution in a uniformly sheared and stratified flow. *J. Fluid Mech.* **342**, 231–261.

KALTENBACH, H.-J., GERZ, T. & SCHUMANN, U. 1994 Large-eddy simulation of homogeneous turbulence and diffusion on stably stratified shear flow. *J. Fluid Mech.* **280**, 1–40.

KERR, R. 1985 Higher order derivatives, correlations and the alignment of small scale structures in isotropic numerical turbulence. *J. Fluid Mech.* **153**, 31–58.

KERR, R. 1987 Histograms of helicity and strain in numerical turbulence. *Phys. Rev. Lett.* **59**, 783–786.

KLAASSEN, G. & PELTIER, W. 1985a The evolution of finite-amplitude Kelvin–Helmholtz billows in two spatial dimensions. *J. Atmos. Sci.* **42**, 1321–1339.

KLAASSEN, G. & PELTIER, W. 1985b The onset of turbulence in finite-amplitude Kelvin–Helmholtz billows. *J. Fluid Mech.* **155**, 1–35.

KLAASSEN, G. & PELTIER, W. 1989 The role of transverse secondary instabilities in the evolution of free shear layers. *J. Fluid Mech.* **202**, 367–402.

KLAASSEN, G. & PELTIER, W. 1991 The influence of stratification on secondary instability in free shear layers. *J. Fluid Mech.* **227**, 71–106.

Koop, C. & Browand, F. 1979 Instability and turbulence in a stratified layer with shear. *J. Fluid Mech.* **93**, 135–159.

Kraichnan, R. 1968 Small-scale structure of a scalar field convected by turbulence. *Phys. Fluids* **11**, 945–953.

Mahrt, L. & Howell, J. 1994 The influence of coherent structures and microfronts on scaling laws using global and local transforms. *J. Fluid Mech.* **260**, 247–270.

Majda, A. & Grote, M. 1997 Model dynamics and vertical collapse in decaying, strongly-stratified flows. *Phys. Fluids* A **9**, 2932–2940.

McComb, W. 1990 *The Physics of Fluid Turbulence*. Oxford University Press.

Metcalfe, R., Orszag, S., Brachet, M., Menon, S. & Riley, J. 1987 Secondary instability of a temporally-growing mixing layer. *J. Fluid Mech.* **184**, 207–243.

Miles, J. 1961 On the stability of heterogeneous shear flows. *J. Fluid Mech.* **10**, 496–508.

Mjolsness, R. 1975 Diffusion of a passive scalar at large Prandtl number according to the abridged Lagrangian interaction theory. *Phil. Trans. R. Soc. Lond.* A **286**, 125–181.

Moin, P. & Mahesh, K. 1998 Direct numerical simulation: a tool in turbulence research. *Ann. Rev. Fluid Mech.* **30**, 539–578.

Moser, R. & Rogers, M. 1991 Mixing transition and the cascade to small scaline in a plane mixing layer. *Phys. Fluids* A **3**, 1128–1134.

Moser, R. & Rogers, M. 1993 The three-dimensional evolution of a plane mixing layer: pairing and transition to turbulence. *J. Fluid Mech.* **247**, 275–320.

Newberger, P. A. & Caldwell, D. 1981 An inertial subrange in microstructure spectra. *J. Geophys. Res.* **86** (C5), 4265–4268.

Newman, G. & Herring, J. 1979 A test field study of a passive scalar in isotropic turbulence. *J. Fluid Mech.* **94**, 163–194.

Nomura, K. & Elghobashi, S. 1992 Mixing characteristics of an inhomogeneous scalar in isotropic and homogeneous sheared turbulence. *Phys. Fluids* A **4**, 606–625.

Oakey, N. 1982 Determination of the rate of dissipation of turbulent energy from simultaneous temperature and velocity shear microstructure measurements. *J. Phys. Oceanogr.* **12**, 256–271.

Obukhov, A. M. 1949 The structure of the temperature field in a turbulent flow. *Izv. Akad. Nauk. SSSR, Ser. Geogr. Geophys.* **13**, 58–69.

Palmer, T., Fritts, D. & Andreassen, O. 1996 Evolution and breakdown of Kelvin–Helmholtz billows in stratified compressible flows. Part 2: Instability structure, evolution and energetics. *J. Atmos. Sci.* **53**, 3192–3212.

Patnaik, P., Sherman, F. & Corcos, G. 1976 A numerical simulation of Kelvin–Helmholtz waves of finite amplitude. *J. Fluid Mech.* **73**, 215–240.

Peltier, W., Halle, J. & Clark, T. 1978 The evolution of finite-amplitude Kelvin–Helmholtz billows. *Geophys. Astrophys. Fluid Dyn.* **10**, 53–87.

Picirillo, P. & Van Atta, C. 1997 The evolution of a uniformly sheared thermally stratified turbulent flow. *J. Fluid Mech.* **334**, 61–86.

Pierrehumbert, R. & Widnall, S. 1982 The two- and three-dimensional instabilities of a spatially periodic shear layer. *J. Fluid Mech.* **114**, 59–82.

Pope, S. 1990 Lagrangian microscales in turbulence. *Phil. Trans. R. Soc. Lond.* **333**, 309–319.

Qian, J. 1995 Viscous range of turbulent scalar of large Prandtl number. *Fluid Dyn. Res.* **15**, 103–112.

Reutsch, G. R. & Maxey, M. 1992 The evolution of small-scale structures in homogeneous, isotropic turbulence. *Phys. Fluids* A **4**, 2747–2760.

Rogers, M. & Moser, R. 1992 The three-dimensional evolution of a plane mixing layer: the Kelvin–Helmholtz rollup. *J. Fluid Mech.* **243**, 183–226.

Rohr, J., Itsweire, E., Helland, K. & Van Atta, C. 1988 Growth and decay of turbulence in a stably stratified shear flow. *J. Fluid Mech.* **195**, 77–111.

She, Z.-S., Jackson, E. & Orszag, S. 1991 Structure and dynamics of homogeneous turbulence: models and simulations. *Proc. R. Soc. Lond.* A **434**, 101–124.

Smyth, W. 1992 Spectral transfers in two-dimensional anisotropic flow. *Phys. Fluids* A **4**, 340–349.

Smyth, W. & Moum, J. 1999a Evolution of turbulence in stably stratified mixing layers. Part 1: Length scales. *Phys. Fluids* A (submitted).

Smyth, W. & J. Moum, J. 1999b Evolution of turbulence in stably stratified mixing layers. Part 2: Anisotropy. *Phys. Fluids* A (submitted).

SMYTH, W. & PELTIER, W. 1989 The transition between Kelvin–Helmholtz and Holmboe instability: and investigation of the overreflection hypothesis. *J. Atmos. Sci.* **46**, 3698–3720.

SMYTH, W. & PELTIER, W. 1991 Instability and transition in Kelvin–Helmholtz and Holmboe waves. *J. Fluid Mech.* **228**, 387–415.

SMYTH, W. & PELTIER, W. 1993 Two-dimensional turbulence in homogeneous and stratified shear layers. *Geophys. Astrophys. Fluid Dyn.* **69**, 1–32.

SORIA, J., SONDERGAARD, R., CANTWELL, B., CHONG, M. & PERRY, A. 1994 A study of the fine-scale motions of incompressible, time-developing mixing layers. *Phys. Fluids* A **6**, 871–884.

SUN, C., SMYTH, W. & MOUM, J. 1998 Dynamic instability of stratified shear flow in the upper equatorial Pacific. *J. Geophys. Res.* **103**, 10323–10337.

TENNEKES, H. & LUMLEY, J. 1972 *A First Course in Turbulence*. MIT Press.

THORODDSEN, S. & VAN ATTA, C. 1996 Experiments on density-gradient anisotropies and scalar dissipation of turbulence in a stably stratified fluid. *J. Fluid Mech.* **322**, 383–409.

THORPE, S. 1973 Turbulence in stably stratified fluids: a review of laboratory experiments. *Boundary-Layer Met.* **5**, 95–119.

THORPE, S. 1987 Transition phenomena and the development of turbulence in stratified fluids. *J. Geophys. Res.* **92**, 5231–5245.

TSINOBER, A., KIT, E. & DRACOS, T. 1992 Experimental investigation of the field of velocity gradients in turbulent flows. *J. Fluid Mech.* **242**, 169–192.

VINCENT, A. & MENEGUZZI, M. 1991 The spatial structure and statistical properties of homogeneous turbulence. *J. Fluid Mech.* **225**, 1–20.

WERNE, J. & FRITTS, D. 1999 Stratified shear turbulence: evolution and statistics. *Geophys. Res. Lett.* **26**, 439–442.

WILLIAMS, R. & PAULSON, C. 1977 Microscale temperature and velocity spectra in the atmospheric boundary layer. *J. Fluid Mech.* **83**, 547–567.

YEUNG, P. & BRASSEUR, J. 1991 The response of isotropic turbulence to isotropic and anisotropic forcing at the large scales. *Phys. Fluids* A **3**, 884–897.

YEUNG, P., BRASSEUR, J. & WANG, Q. 1995 Dynamics of direct large-small scale couplings in coherently forced turbulence: concurrent physical- and Fourier-space views. *J. Fluid Mech.* **283**, 43–95.

YEUNG, P., GIRIMAJI, S. & POPE, S. 1990 Straining and scalar dissipation on material surfaces in turbulence: implications for flamelets. *Combustion Flame* **79**, 340–365.